



Department of Materials Science and
Engineering
The University of Michigan
2300 Hayward
Ann Arbor, MI 48109-2136

Low-Cost Mg Sheet Component Development and Demonstration Project DE-EE-0007756: Task 2.2 Dynamic Recrystallization, Texture, and Grain Growth

Final Report to USAMP
Reporting Period: Oct 1st, 2016 – Jan 28th, 2021

Performing Organization & Address: The University of Michigan

Principal Investigator: Professor John Allison

Co-authors: Tracy Berman

Disclaimer 1: "This report was prepared as an account of work sponsored by an agency of the United States Government. Neither the United States Government nor any agency thereof, nor the USCAR-USAMP LLC, or any of their employees, makes any warranty, express or implied, or assumes any legal liability or responsibility for the accuracy, completeness, or usefulness of any information, apparatus, product, or process disclosed, or represents that its use would not infringe privately owned rights. Reference herein to any specific commercial product, process, or service by trade name, trademark, manufacturer, or otherwise does not necessarily constitute or imply its endorsement, recommendation, or favoring by the United States Government or any agency thereof. The views and opinions of authors expressed herein do not necessarily state or reflect those of USCAR-USAMP, the United States Government or any agency thereof."

Disclaimer 2: "This technical report does not contain any of the following: limited rights data (proprietary data), classified information, protected PII, information subject to export control classification, or other information not subject to release."

Acknowledgement and List of Content Contributors/Co-Authors

- a. **Acknowledgement:** This material is based upon work supported by the Department of Energy, Office of Energy Efficiency and Renewable Energy (EERE), under Cooperative Agreement Award Number DE-EE007756 with the United States Council for Automotive Research's consortium The United States Automotive Materials Partnership (USAMP LLC); It was performed by The University of Michigan under USAMP subaward during 2016 – 2021
- b. We also gratefully acknowledge Professor Michelle Manuel of University of Florida who provided the cast plates.

List of abbreviations:

EBSD: Electron Backscatter Diffraction
IPF: Inverse Pole Figure
RX: recrystallized/recrystallization
DRX: dynamic recrystallization
DDRX: discontinuous dynamic recrystallization
SRX: static recrystallization
PSC: Plane strain compression
GB: grain boundary
GOS: grain orientation spread
GAM: grain average misorientation
MRD: multiples of random density
JMAK: Johnson-Mehl-Avrami-Kolmogorov recrystallization model
HCP: hexagonal close packed
TMP: thermomechanical processing/process

Executive Summary:

It has been previously established that the RE-like textures associated with improved formability in Mg alloy sheets can also be produced using Mg-Zn-Ca alloys [1–7], but the mechanisms responsible are still not fully understood. A more complete understanding of the mechanisms and kinetics of recrystallization and grain growth in these alloys will provide the foundation for developing ICME tools to predict the microstructure and texture development that occurs during sheet rolling and sheet forming operations. These ICME tools can be used to develop and refine the next generation of formable Mg alloys and optimize key processing variables. In particular, the role of the Zn and Ca solutes needs to be better understood in order to design alloys with wide processing windows that are suitable for industrial use. Though several promising Mg-Zn-Ca alloys are described in literature, it is difficult to make comparisons when the alloys have undergone different processing routes. Producing formable Mg alloy sheets requires having both the correct alloy and the correct TMP route for that alloy; improper processing can result in the strong basal texture known to be detrimental to through-thickness sheet formability.

This study explores the texture and microstructure of thermomechanically processed unalloyed Mg, Mg-Ca binary alloys, and Mg-Zn-Ca ternary alloys. A Gleeble 3500 thermomechanical processing simulator was used to physically simulate the rolling process, allowing for careful control of conditions so that processing paths can more accurately be coupled to the resulting microstructure. Primarily optical microscopy and EBSD mapping were used for characterization. In particular, the EBSD Grain Orientation Spread technique was used to distinguish between recrystallized and deformed grains.

Of all of the alloy and TMP routine combinations used in this work, the Mg-3.2Zn-Ca alloys exhibited the weakest textures with an annular structure in the basal pole figures. This texture is consistent with what is required for a formable Mg alloys sheet. These alloys contained the highest Zn content included in this study. To achieve the desirable texture, the alloy must contain at least 0.1 weight percent Ca however Ca content above this level had little effect on the texture in the alloys explored in this study. Processing in an alloy with Mg-2.1Zn-0.1 Ca was also able to be optimized to produce the desirable texture as described below.

Several factors were found to be important when designing the optimum TMP schedule. The processing schedule that produced the most desirable texture consisted of ten passes with a constant true strain of 0.2 per pass at a strain rate of 0.5s^{-1} . Between passes the specimens were held at 350°C for 10 minutes, a step which is referred to as the intermediate anneal throughout this work. After the 10th pass, the three higher Zn-content alloys exhibited a relatively low (<5 MRD) basal texture compared to the other alloys studied. At this stage the Mg-3.2Zn-Ca alloys exhibited a low fraction of recrystallized grains. A final post-deformation annealing treatment of 30 minutes at 350°C resulted in complete recrystallization in the higher Zn ternary alloys, leading to the development of the weak, annular basal texture in the alloys with 3.2 wt% Zn.

When developing the optimized TMP schedule, the effect of several processing variables were explored. High strain rates (1s^{-1} in the Mg-Zn-Ca system with a 350°C deformation temperature) led to strain localization and inhomogeneous microstructures in which basal grains were often prevalent. Small reductions per pass promoted abnormal growth of basal grains. The thermal soak between passes was also found to be critical. The samples with the weakest final textures underwent very little grain growth during these intermediate annealing treatments. These samples also consisted primarily of grains with a high degree of internal misorientation and contained a low fraction of recrystallized grains in the as-deformed state.

The RX grains that do exist in the as-deformed state in the weakly-textured materials are small grains found primarily along grain boundaries. These grain boundaries are serrated in nature and grain boundary bulging is clearly one mechanism for the formation of RX grains in these alloys. These microstructural features are signatures of discontinuous dynamic recrystallization (DDRX). The small RX grains have random orientations and were found to exist in all stages of the processing, from the 1st deformation pass to the 10th deformation pass and beyond. Limited grain growth and recrystallization occurred during the annealing step between passes, suggesting restricted grain boundary mobility, which, when combined with the serrated grain boundaries, demonstrates that solutes pinning is an active mechanism in the weakly-textured Mg-Zn-Ca samples.

The result of the limited grain growth and static recrystallization between passes is that the microstructure after deformation consists of larger, deformed grains surrounded by a necklace structure of small RX grains. It was established that these deformed grains ($\text{GOS} > 1^\circ$) tend to have near-basal orientations. During the final recrystallization annealing treatment, the deformed grains are consumed by the more randomly oriented RX grains, resulting in the desired decrease in basal texture intensity.

Not all alloys studied demonstrated texture improvement during the final annealing treatment. In the unalloyed Mg, the Mg-Ca binaries, and the Mg-0.5Zn-0.1Ca ternary (the ternary with the lowest Zn content in this study) the strong (> 12 MRD) basal texture in the as-deformed state was unchanged after annealing at 350°C for 30 minutes. These alloys showed no evidence of DDRX. A population of randomly-oriented RX grains did not exist after ten deformation passes in these alloys, resulting in a strong texture in the as-deformed condition. With no mechanism for introducing randomly oriented grains during the final annealing treatment, the strong basal texture was retained. This lack of texture evolution is consistent with literature on conventional Mg alloys such as AZ31.

The ZX21 alloy also did not initially demonstrate texture improvement after the final annealing treatment. Unlike the more-dilute alloys in the previous paragraph, the final as-deformed microstructure in ZX21 did contain a population of randomly-oriented DRX grains. Given the existence of these RX grains and promising results on this alloy in the literature, the TMP routine was varied in this alloy in an attempt to produce a weaker final texture. These routines were designed with the intent to limit SRX and grain growth during the intermediate annealing treatments. This approach successfully led to an improved final texture and suggests opportunities for further texture optimization in this alloy.

While limiting SRX and grain growth during the intermediate annealing treatments can lead to favorable changes in the final texture, if adequate process control is not used it is possible to produce an undesirable texture. It was demonstrated that increasing the duration of the intermediate annealing step in ZX30 lead to an increase in the final texture intensity. It also, not unexpectedly, led to an undesirable increase in the final grain size. Understanding the kinetics of static recrystallization and grain growth in these alloys is essential for microstructure and texture optimization. Previous studies on Mg-Zn-Ca alloys support the conclusion that grain nucleation and growth are important mechanisms, however much of the focus has been on nucleation in twins and band-like structures [8].

The database from USAMP and mechanistic studies will serve as a strong foundation for important further ICME work on recrystallization. There is still a need for models for both deformed texture and recrystallization texture in Mg alloys. It should be possible to model the deformation component of texture evolution by coupling the critical resolved shear stress determined using Density Functional Theory (DFT) calculations with crystal plasticity modeling. Modeling the recrystallization component of the texture requires ICME models for DRX, SRX, and grain growth kinetics. These RX models remain a gap, but the USAMP project has provided a strong foundation for their further development.

Materials and Experimental Approach :

Cast ingots with dimensions of approximately 80 mm x 80 mm x 20 mm were received from the University of Florida. A summary of the compositions studied is shown in Table I. The binary ingots were solution treated for 24 h at 500°C, while the ternary ingots were solution treated for 24 h at 350°C. The unalloyed Mg was used in the as-cast condition. Plane strain compression (PSC) samples with dimensions of 20 mm x 15 mm x 10 mm were extracted from the center regions of the ingots. Figure 1 provides a comparison of the initial microstructure in the PSC samples. The grain size is on the order of mm and some porosity was present. Samples obviously containing porosity were discarded.

Table I: Alloy designation and composition as measured using OES at Ford Motor Co.

Alloy name	Zn content (wt %)	Ca content (wt %)
Unalloyed	0	0
X0	0	0.1
X1	0	0.3
ZX0p50	0.5	0.1
ZX10	1	0.1
ZX21	1.9	0.3
ZX30	3.2	0.1
ZX31	3.2	0.3

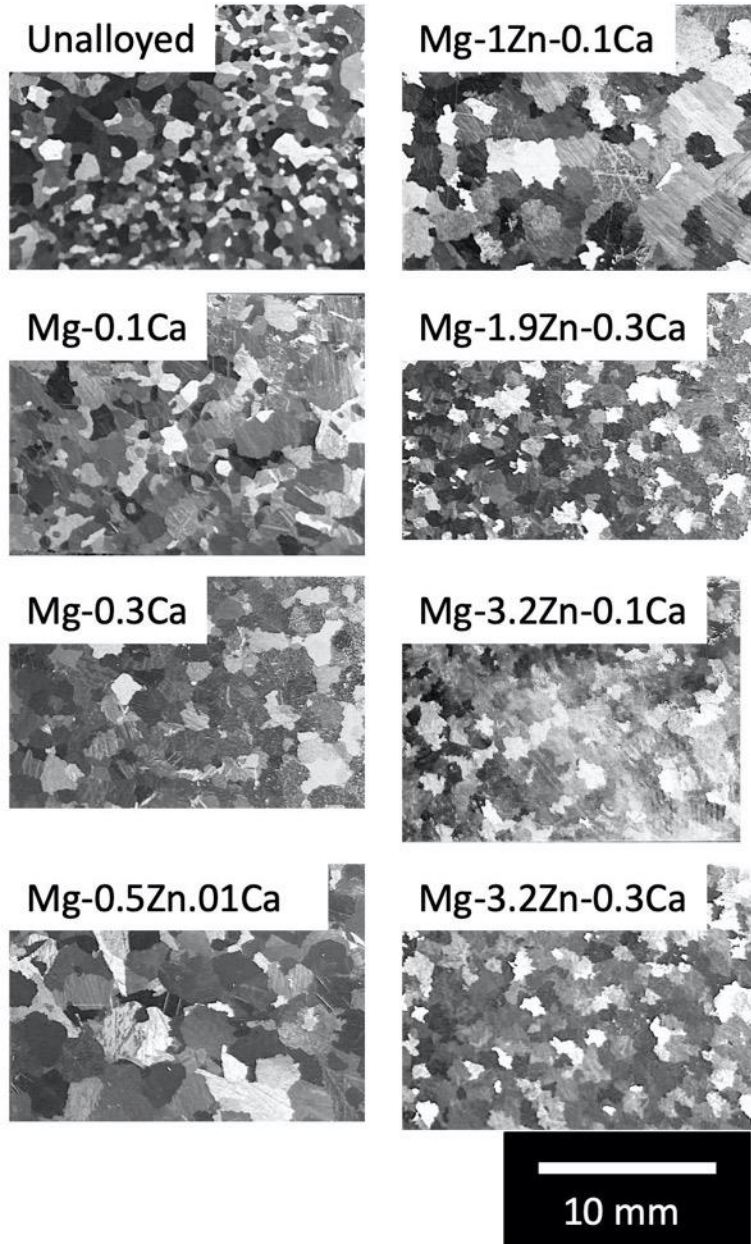


Figure 1: Photographs comparing the structure of the alloys prior to Gleeble testing.

Testing was conducted using a Gleeble Model 3500 thermo-mechanical simulator with two k-type thermocouples spot-welded to the sample surface (one at mid-height and a second at quarter height). Several different TMP routines were employed in this work. Those most significant to this work are summarized in Table II. The complete Gleeble program files can be found in the Materials Commons. For all TMP schedules, the samples were heated up to 350°C at a rate of 5°C/s and then held at 350°C for 10 minutes before the first compressive hit. The temperature was held at that constant temperature during the entire processing routine, including the thermal soaks between passes (referred to as the intermediate annealing step). Most specimen were air quenched within the Gleeble system following the final hit. These specimens were cut in half, and generally one half was studied in the as-deformed state while the other was

annealed in a box furnace and water quenched. In some of the earlier tests the final annealing treatment was performed in the Gleeble, this will be noted in the sample description.

Table II: Summary of Gleeble PSC TMP routines used in this work

Process Name	# of passes	Temp (°C)	Strain Rate (s ⁻¹)	Strain per Pass	Duration of intermediate anneal (s)
10-pass	10	350	0.5	0.2	600
1-pass	1	350	0.5	0.2	600
3-pass	3	350	0.5	0.2	600
5-pass	5	350	0.5	0.2	600
10-pass (15s)	10	350	0.5	0.2	15
10-pass (5min)	10	350	0.5	0.2	300
10-pass (30 min)	10	350	0.5	0.3	1800
Ramp	12	350 to 325	0.5	0.5 to 0.25	300
20-pass	20	350	1	0.03 to 0.4	300
20-pass (15s)	20	350	1	0.03 to 0.4	15
10-pass (0.1s ⁻¹)	10	350	0.1	0.2	600
10-pass (0.25s ⁻¹)	10	350	0.25	0.2	600
10-pass (1s ⁻¹)	10	350	1	0.2	600

Optical microscopy and electron backscatter diffraction (EBSD) mapping were used for characterization. The samples were mounted such that the compression direction was normal to the grinding surface. Polishing was conducted using diamond paste and an oil-based lubricant. For optical microscopy, the samples were etched in a solution of 10 mL water, 10 mL acetic acid, 4.3 g of picric acid (crystals), and 70 mL of ethanol for approximately three to five seconds. The final preparation step before EBSD was etching for approximately five seconds in a solution of 60 mL ethanol, 20 mL water, 15 mL glacial acetic acid, and 3 mL of nitric acid.

EBSD was conducted using a Tescan Mira3 electron microscope operated at 30keV with a beam intensity setting of 20. In most cases, multiple scans were collected for each specimen. Smaller, higher resolution scans were used to study grain size and morphology and to determine the extent recrystallization. Larger scans were used to determine crystallographic texture. These scans were collected using a step size of 3 μm and represent an area of at least 2mm² unless otherwise specified. MTEX[9] was used to calculate the texture from the EBSD scans. Data points with a confidence index less than 0.1 were excluded from analysis.

Effect of alloying:

The effect of solutes in Mg-Ca and Mg-Zn-Ca alloys on the texture and microstructure was studied using the 10-pass process (refer to Table II). This thermomechanical processing routine used consisted of 10 compressive hits of equal strain (0.2) resulting in a thickness reduction from 10 mm to approximately

1.8mm. After the final hit, all specimens were air quenched within the Gleeble system for 30 s. The deformed specimens were cut in half. One portion of each sample was annealed for 30 minutes at 350°C in a small box furnace followed by a water quench.

The Gleeble true stress – true strain responses for all alloys are presented in Figure 2(a). Though there is some scatter between the tests, the strain achieved at each pass and the total strain for all samples is relatively consistent. As expected, the ternary alloys exhibit a higher stress during compression than the dilute alloys. The temperature profiles from the thermocouple mounted in the deformed region of all specimen are consistent (Figure 2(b)), demonstrating that all samples were subjected to the same thermal environment. The blips in the temperature are coincident with the compressive hits, after which the Gleeble quickly returned each sample to the set temperature of 350°C as measured by a second thermocouple outside the deformation region. The cooling rate during the post-deformation air quench was approximately 7°C per second.

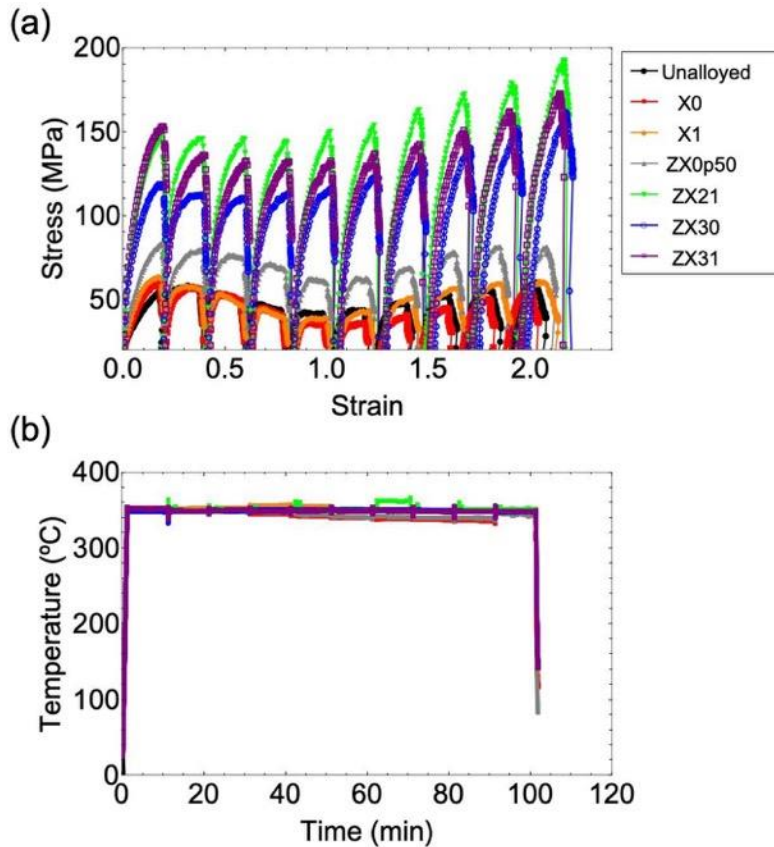


Figure 2: (a) Gleeble true stress-true strain plot and (b) temperature profile during testing Gleeble testing for the seven specimens.

After deformation, the unalloyed Mg, binary alloys, and the low Zn ternary have an inhomogeneous microstructure consisting of bands of finer grains surrounded by larger grains, as illustrated by the optical micrograph of the X0 alloy in Figure 3 (a). In contrast, the higher-Zn ternary alloys have a finer and more consistent grain size through the reduced section, with a mean grain diameter of approximately 20 μm as can be seen in the ZX30 alloy in Figure 3 (b). As processing for all alloys was fixed, the grain refinement and more homogenous as-deformed microstructure in Figure 3(b) compared to Figure 3(a) must be an effect of the addition of 3.2 wt% Zn to Mg-0.1Ca.

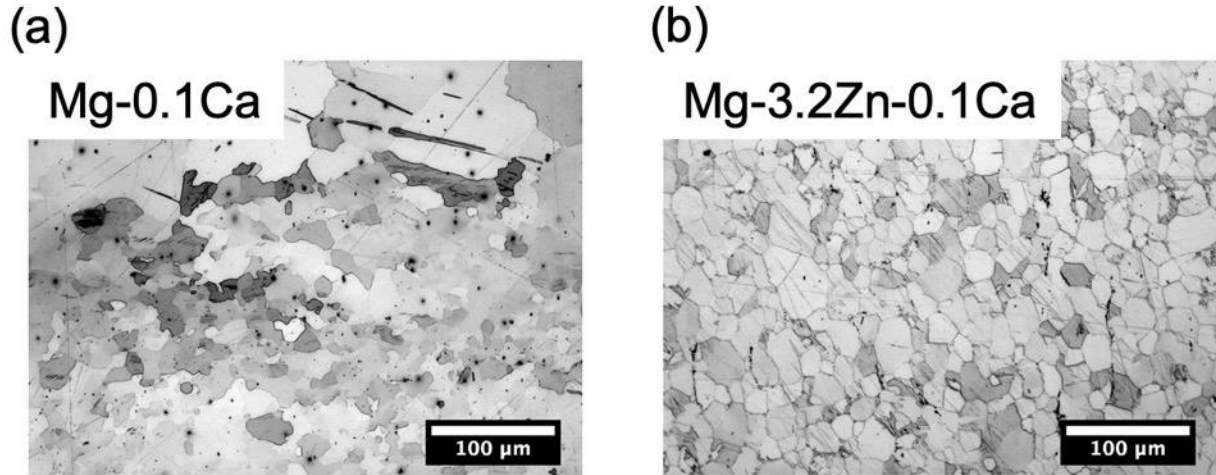


Figure 3: Optical micrographs of the (a) deformed Mg-0.1Ca binary and the (b) deformed Mg-3.2Zn-0.1Ca ternary alloy. The rolling direction is vertical. Correction: Scale bar units should read 200 μm .

Higher magnification microscopy reveals a second difference in the deformed condition; the three higher-Zn ternary alloys have exhibit serrated grain boundaries, evidence of grain boundary bulging, and sub-micron grains decorating the boundaries of some of the larger grains (Figure 4(a)). These features are considered characteristics of discontinuous dynamic recrystallization (DDRX) [10]. The grain boundary structures in the other alloys and in unalloyed Mg are fairly straight, even in the finer-grained regions highlighted in Figure 4(a).

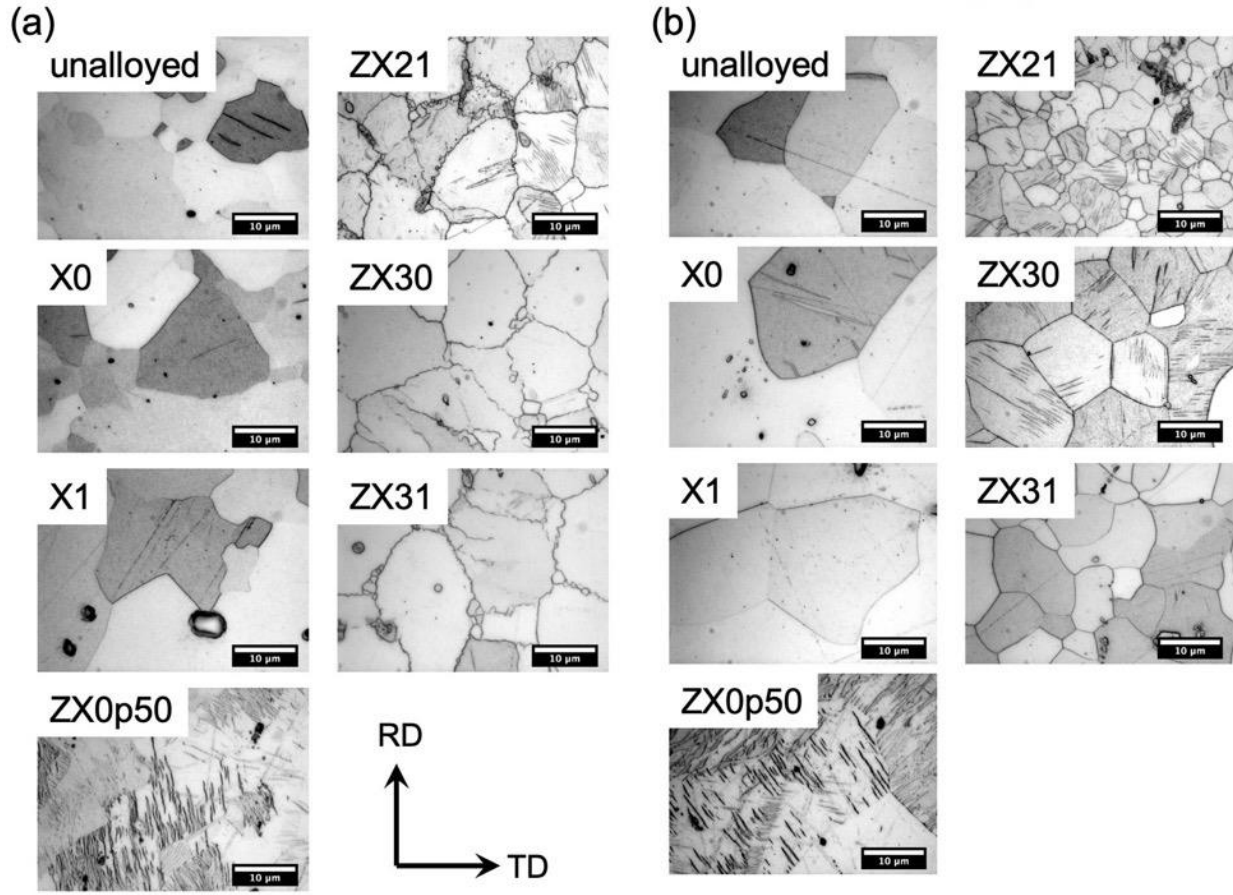


Figure 4: Optical micrographs illustrating the microstructure of the samples in the (a) as-deformed and (b) annealed conditions. Correction: Scale bar units should read 20 μm .

EBSD GOS spread maps (Figure 5) illustrate differing amounts of recrystallization (RX) in the as-deformed state. Given the inhomogeneity in the dilute materials, the maps shown for these materials in Figure 5 should not be interpreted as completely representative of the microstructure, but it is clear the bulk of these materials are in a deformed, unrecrystallized state. More quantitative information can be drawn from the higher Zn ternary alloys. GOS maps of the ZX21 sample showed bands of grains with a misorientation of 1° or less. Using 1° as the cutoff between deformed and recrystallized grains[11,12], the ZX21 sample is $\sim 40\%$ recrystallized. The two alloys with 3.2 wt% Zn are less than 1% RX after 10 hits.

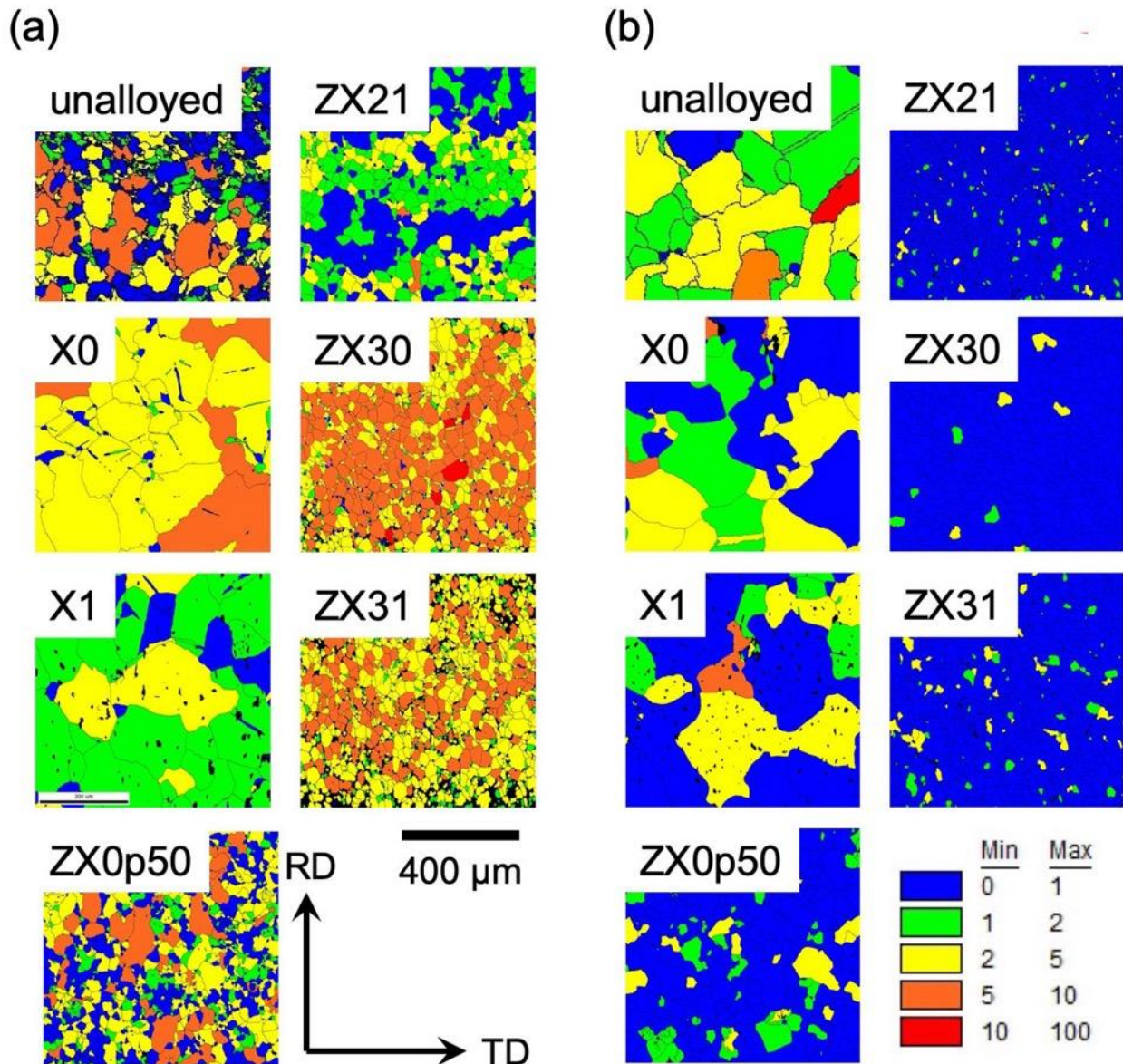


Figure 5: EBSD GOS maps of the samples in the (a) as-deformed and (b) annealed conditions. All maps cover an area of 800 $\mu\text{m} \times 800 \mu\text{m}$.

The post-deformation annealing treatment of 30 minutes at 350°C resulted in microstructure evolution in all of the samples (Figure 4 and Figure 5). The average grain diameter (as measured from the EBSD maps) increased to approximately 60 μm in the dilute alloys. The EBSD GOS maps (Figure 5) demonstrate that, while the amount of misorientation decreased in the dilute materials, the post-deformation annealing treatment did not lead to complete SRX. Histograms of the GOS distribution in the materials, shown in Figure 6, show little evolution in grain misorientation in the unalloyed Mg and only a slight shift to lower internal misorientations in the binary alloys.

The final annealing treatment resulted in more extensive static recrystallization (SRX) in the three higher Zn ternary alloys. The faster recrystallization kinetics in these alloys is consistent

with their finer as-deformed grain size[12]. The microstructure of all three of these alloys consists primarily of equiaxed grains with low internal misorientation (Figure 4(b) and Figure 5(b)). Unlike in the dilute materials, the annealing treatment did not lead to substantial grain growth. No evolution in grain size is seen in the solute-rich ZX31 alloy. The grain size increases slightly in the ZX30 alloy (which contains the lowest wt% Ca of the ternaries) from 20 μm to just under 30 μm . Based on the 800 $\mu\text{m} \times 800 \mu\text{m}$ EBSD maps, which contain over 700 grains each, the grain diameter in ZX21 appears to decrease from 25 μm in the deformed condition to 12 μm in the annealed condition.

Histograms comparing the GOS evolution after the 30-minute annealing treatment are shown in Figure 6. The GOS distribution is comparable for all three of the higher Zn ternary alloys after annealing. In the as-deformed condition, the 3.2 wt% Zn alloys contain a larger number fraction of grains with a high internal misorientation. The distribution of GOS values in ZX30 and ZX31 is centered a few degrees higher, and is broader, than that measured in the ZX21 sample.

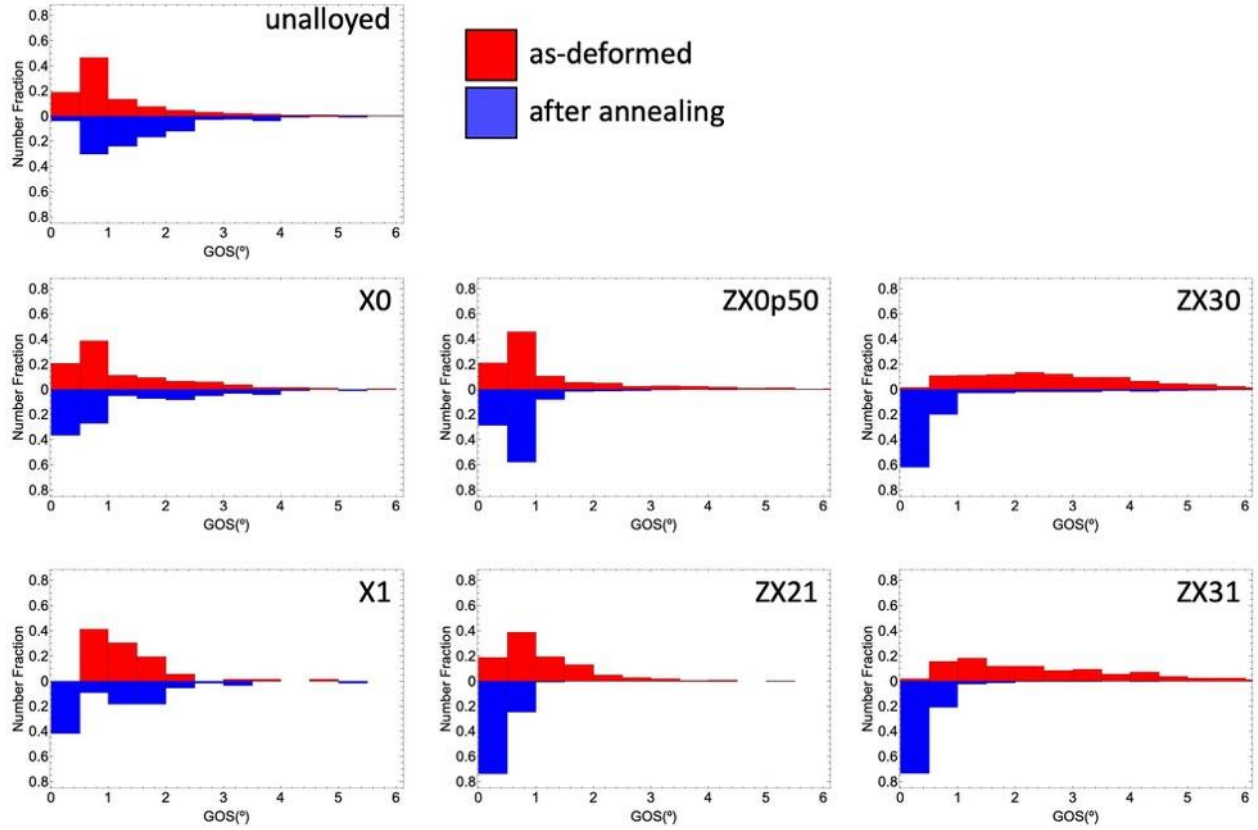


Figure 6: Histograms comparing the evolution of GOS after annealing in the seven alloys.

The as-deformed and post-annealing textures in dilute alloys and the ternary alloys are quite different, and therefore different scale bars are used for the two sets of materials in Figure 7. The dilute alloys all exhibit a strong basal texture, with a maximum intensity greater than 12

multiples of random density (MRD), in the deformed condition (Figure 7(a)). Annealing for 30 minutes did not lead to any appreciable change of texture in these alloys.

The higher Zn ternary alloys all exhibited comparatively weak textures in the deformed state, with maximum basal pole figure intensities in the range of 3 to 5 MRD (Figure 7(b)). The basal poles in these alloys are slightly spread in the transverse direction. In ZX21, the texture was largely unchanged by annealing. In the 3.2 wt% Zn alloys, the final annealing treatment lead to a significant change in texture. During static recrystallization, the c-axis of the grains tilted down away from the sample normal, resulting in an annulus around the basal pole and a decrease in the maximum basal pole figure intensity to ~ 2 MRD.

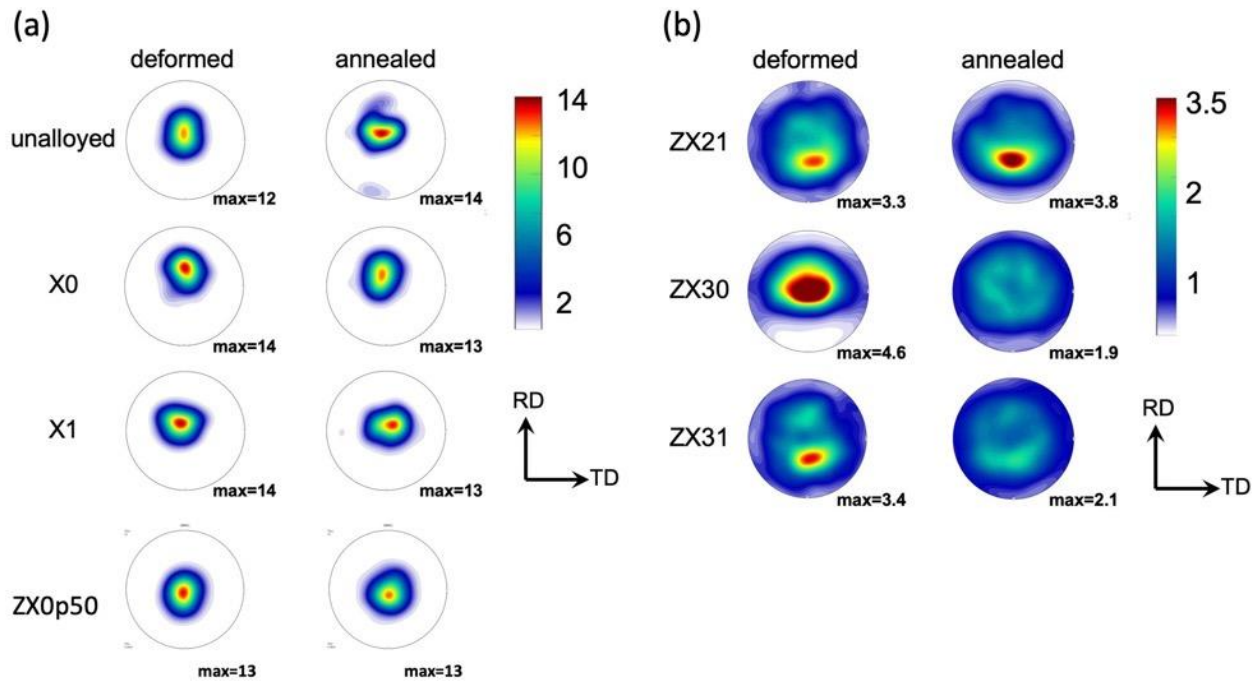


Figure 7: Basal (0001) pole figures of the (a) unalloyed Mg, Mg-Ca binary alloys and the low-Zn ternary alloy and (b) the higher Zn Mg-Zn-Ca ternary alloys in the as-deformed and annealed conditions

The higher Zn ternary alloys exhibited much different microstructure and texture behavior during TMP and annealing than the Zn free and low Zn alloys. Relatively weak basal textures were produced higher Zn ternary alloys. This is consistent with existing literature that demonstrates that alloying with Zn + (RE, Ca) can prevent the development of strong basal and RD-split basal textures typically seen in AZ31[1,6,7,13,14]. The addition of Ca alone did not change the texture evolution from that observed in unalloyed Mg in this study, though Lee et al [15] did observe basal texture reduction during SRX in the same binary alloys. The Zn content had a much stronger effect on the texture evolution than the Ca content. The behavior of ZX30 and ZX31 are quite similar, despite the higher Ca content in ZX31. In contrast, ZX21 and ZX31, which vary in composition by ~1 wt% Zn, responded differently to both TMP and the post-deformation annealing treatment.

Evidence of discontinuous DRX (DDRX) was observed in the microstructures of all three ternary alloys. DDRX results when local grain boundary bulging leads to a decrease in dislocation density, acting as a nuclei for recrystallized grains that can consume adjacent deformed grains[10]. This mechanism is not associated in a significant change in texture; however the alloys which exhibited DDRX were also the alloys with a significantly weaker texture after 10 passes. Reduced mobility of high-angle grain boundaries due to solute drag may have arrested DDRX and allowed for the higher grain misorientations observed in ZX30 and ZX31 GOS maps.

Multiple mechanisms contribute to the texture in the as-deformed state. One contribution is the texture that results from deformation itself. Alloying with Zn + Ca has been demonstrated to promote non-basal slip activity [16], and therefore weaker deformation textures are expected in the ternary alloys. Texture evolution resulting from the DRX can affect the texture in the as-deformed state as well. In addition, SRX that occurs during the thermal soaks between passes can also contribute to texture evolution. It is difficult to determine the relative contribution of each of these mechanisms in ex-situ studies such as this one, though computational simulations may be used to decouple them in the future.

It is important to note that only the alloys with microstructures consisting of a large fraction of highly misoriented grains underwent a change in texture during annealing. Retardation of recrystallization kinetics provides for an accumulation of internal grain misorientation during the multi-step deformation process, this allows for more extensive SRX in the final annealing treatment. Bohlen et al [7] tracked the texture evolution during static recrystallization at 400°C in hot-rolled Mg-0.91 wt% Zn -0.52 wt% Ca alloy and also observed texture reduction, which they attributed to more randomly oriented RX grains consuming more strongly textured deformed grains. This is consistent with the observations in the current study, particularly that the samples that underwent the most SRX also exhibited the largest texture reduction. Bohlen et al associated the randomly nucleated grains with twins in band-like structures, however those features that were not observed using this processing route.

An increased Zn addition seems to retard recrystallization during processing. The deformed ZX21 specimen had a significant fraction of low misorientation grains in the as-deformed state, while the 3.2 wt% Zn alloys had very few recrystallized grains. The TMP schedule used consisted of 10 compressive hits, separated by a 10-minute thermal soak, so post-mortem studies after the complete 10-pass process cannot provide information on relative contributions of static and dynamic recrystallization in the as-deformed structures. However it was shown that, for all alloys studied, DRX grains do not occupy a large fraction of the as-deformed microstructure after 10-passes. This work did not include any Mg-Zn binaries, but literature has not demonstrated a reduction in basal texture intensity during annealing with Zn as the only solute [1,15]. The retarded kinetics may be a result of co-segregation of Zn and Ca atoms to grain boundaries. It has been suggested this co-segregation alters the grain boundary energies and mobilities and limits the growth of basal grains [17]. Future work is needed to explore the mechanisms responsible, but the findings of this study are consistent with conclusions that it is important to retard recrystallization and that alloying with both Zn and Ca is an effective method for doing so.

Effect of total strain (number of passes):

In the previous section, the samples were only studied after ten PSC passes. In order to better understand the evolution through processing, ZX30 samples were tested using the same TMP parameters used in the “10-pass” process but with the samples subjected to fewer total passes (1, 3, and 5). The 1-pass, 3-pass, and 5-pass samples were cut in half in the as-deformed state and one half of each of these samples was annealed at 350°C for 10 minutes before being water quenched. This annealing step is meant to replicate the 10-minute thermal soak that occurs between passes in the standard 10-pass process. As such, the microstructure in the annealed 1-pass sample is equivalent to the microstructure going into the second deformation step. Samples were studied using both optical microscopy and EBSD mapping.

Figure 8 and Figure 9 provide a lower-magnification summary of the microstructure evolution. The microstructure after a single-pass is quite inhomogeneous and twinning is prevalent as a consequence of the large initial grain size. As the number of passes increase, the grain size is refined and becomes more uniform. Regions of larger grains remain after 3-passes, as all of the grains captured are basal in nature, it is possible that deformed basal grains are growing preferentially. As noted earlier in the alloy comparison, little grain growth occurs during annealing of ZX30 at 350°C.

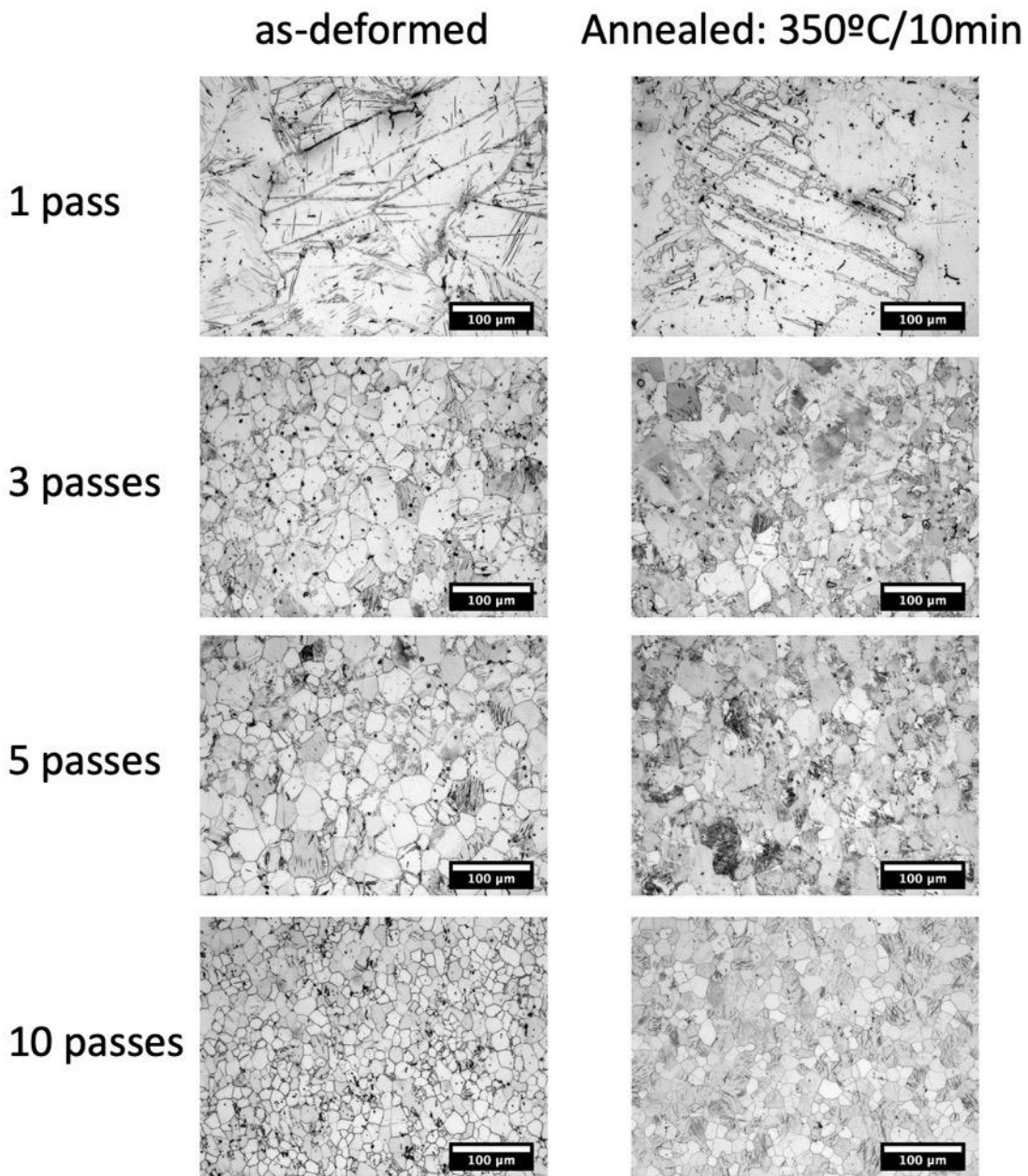


Figure 8: Optical micrographs of ZX30 alloy at various stages along the 10-pass processing route. Correction: Scale bar units should read 200 μm .

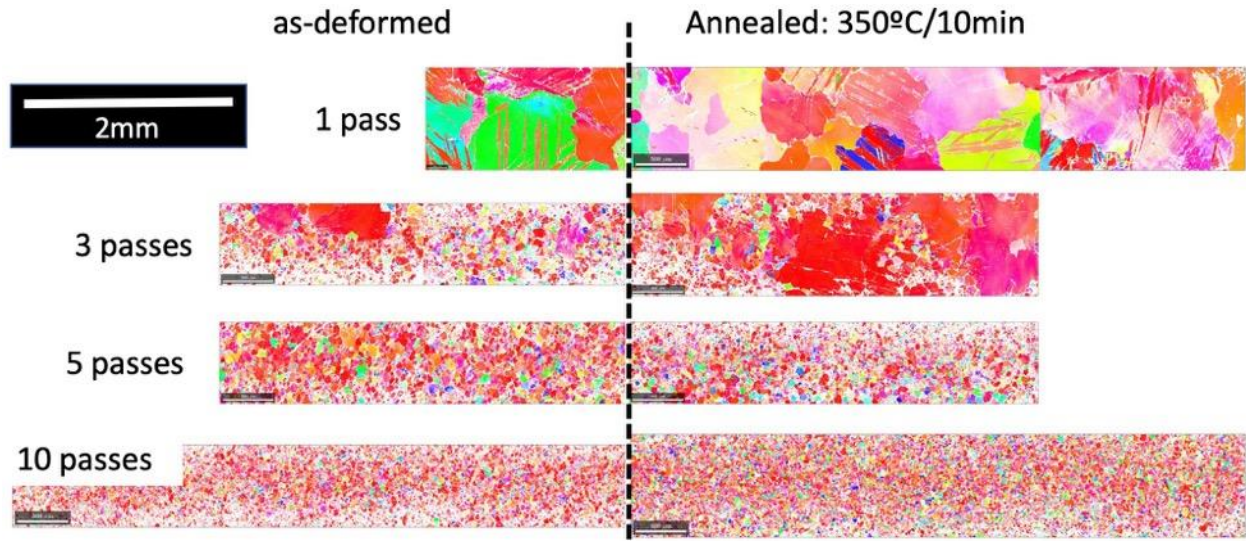


Figure 9: Larger area (lower resolution) EBSD maps collected to calculate texture. All maps are presented using the same scale.

Higher magnification images of the microstructures are shown in Figure 10 and Figure 11, with the focus being on regions with the smaller, presumably RX grains. The higher resolution (but smaller area) EBSD maps were collected on these samples to focus on the grain boundary behavior and the orientation of the finer grains. The twins seen in the 1-pass condition serve as preferential nucleation sites for RX grains in both the as-deformed and annealed conditions. RX grains are found along prior grain boundaries in the as-deformed microstructures with the boundaries of these larger grains being highly serrated. Annealing alleviates some of this grain boundary serration but does not lead to an equiaxed microstructure until after the tenth pass.

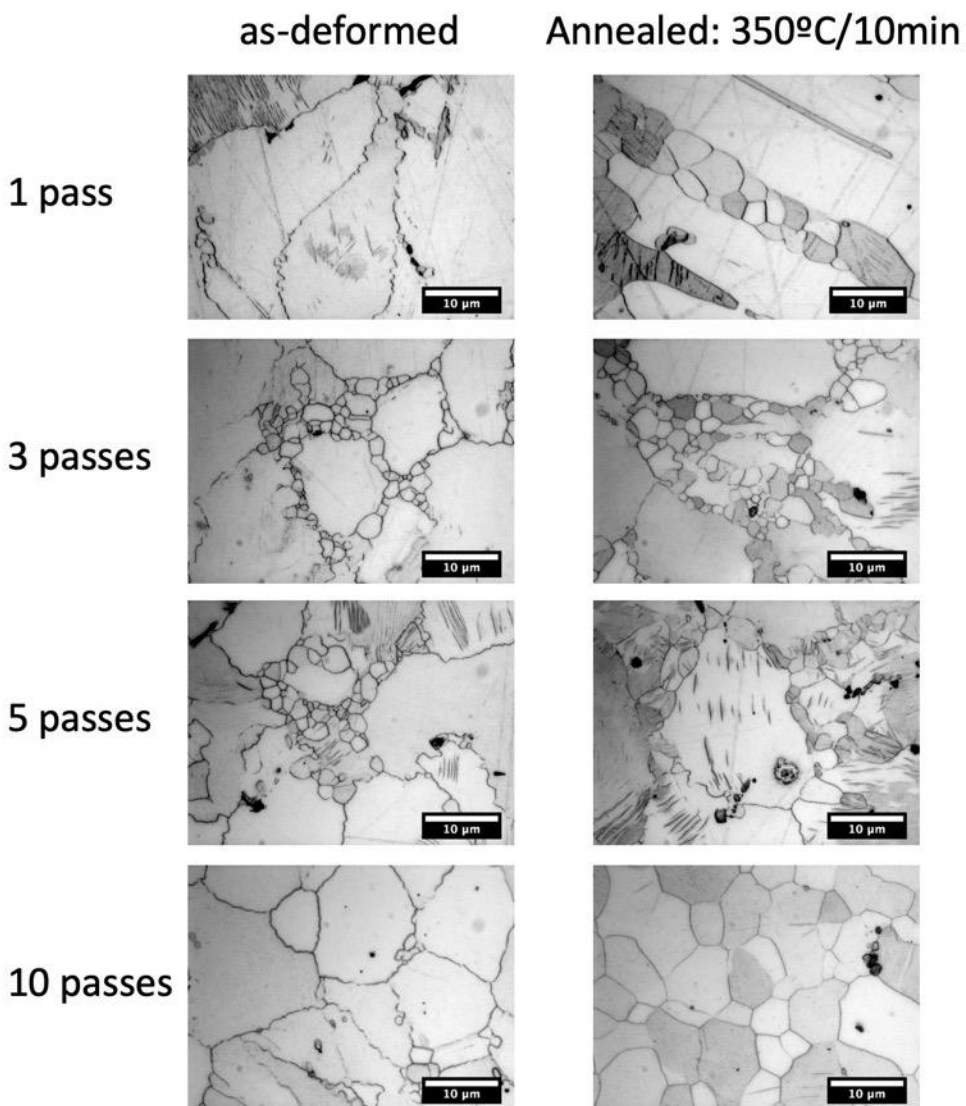


Figure 10: Optical micrographs of ZX30 alloy at various stages along the 10-pass processing route. Correction: Scale bar units should read 20 μm .

as-deformed



annealed: 350°C/10 min

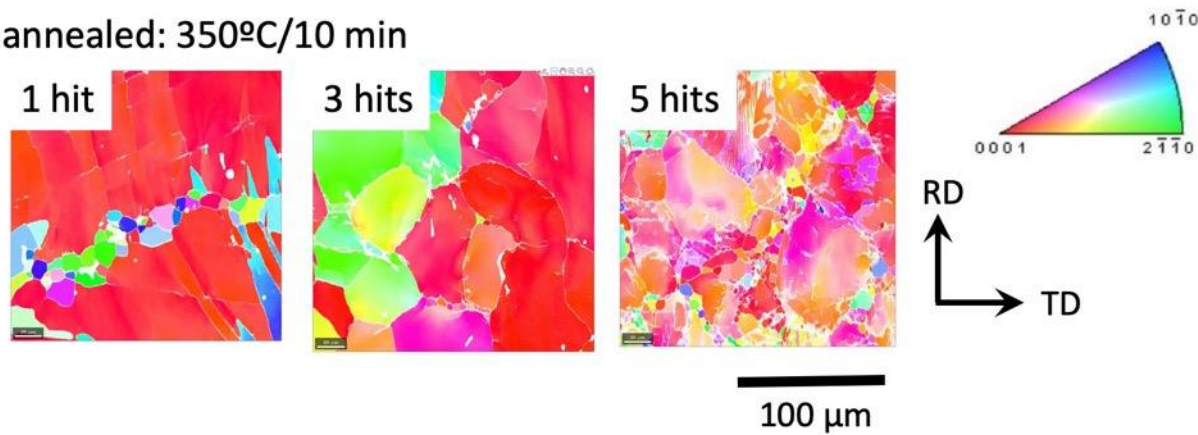


Figure 11: Higher resolution EBSD maps of the ZX30 alloy through the 10-pass process.

The high-resolution EBSD scans do not contain enough grains to calculate a representative texture, but it is helpful to look at discrete grain orientations plotted on an IPF triangle (Figure 12). In these plots, the diameter of the circle correlates the grain area and the color (and location within the IPF triangle) corresponds to average grain orientation. It can be seen that throughout processing, the RX grains are randomly oriented. The RX grains tend to grow during annealing, particularly after the first pass.

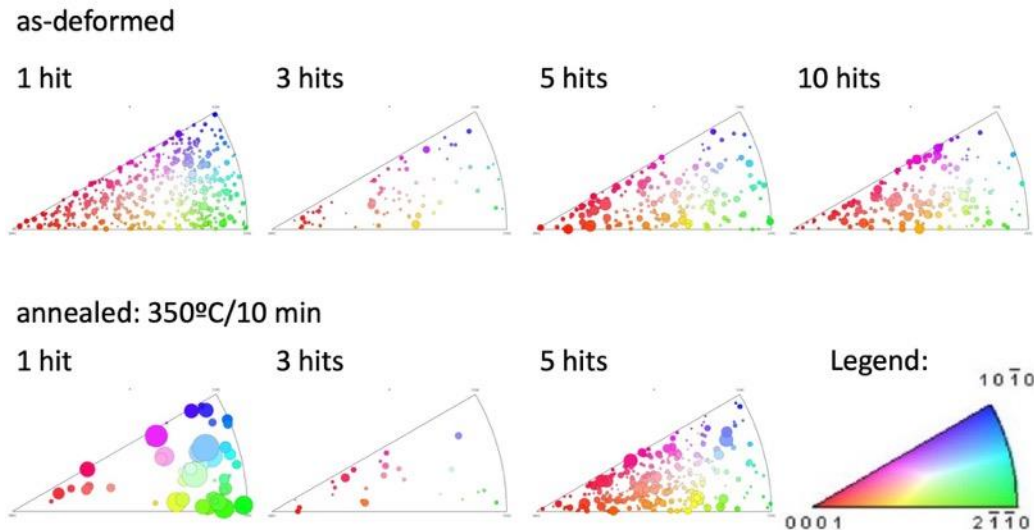


Figure 12: Discrete inverse Pole Figures repetitive to the normal direction for ZX30 samples through the 10-pass process in the (top) as-deformed condition and (bottom) after annealing at 350°C for 10 minutes. The size of the circle corresponds to the grain diameter. The color of the circle corresponds to the grain orientation (redundant information to it's location in the IPF triangle).

Bulk texture was calculated using the lower resolution EBSD scans presented in Figure 9. These maps were collected using a step size of 3 μm in order to sample a representative number of grains (for the samples with 3 or more passes) and so it should be noted that there will be a tendency for the small RX grains to be missed, especially in the as-deformed condition where they are smaller. Not enough grains were sampled in the 1-pass sample for the texture intensity to be significant (many measurements of large grains will create “hot spots” in the pole figures) but it is interesting to note the evident peaks from twinning in the deformed condition. The larger grains in the 3-pass conditions also lead to more intense texture. It is not until the grain size becomes more uniform and refined after 5-passes that the texture weakens to ~ 4 MRD. As discussed earlier, the final RX anneal after 10-passes is essential to producing the weakest texture. In Figure 13, the final annealing step was 10 minutes at 350°C. It was previously demonstrated that 30 minutes leads to complete RX and further reduces the basal intensity.

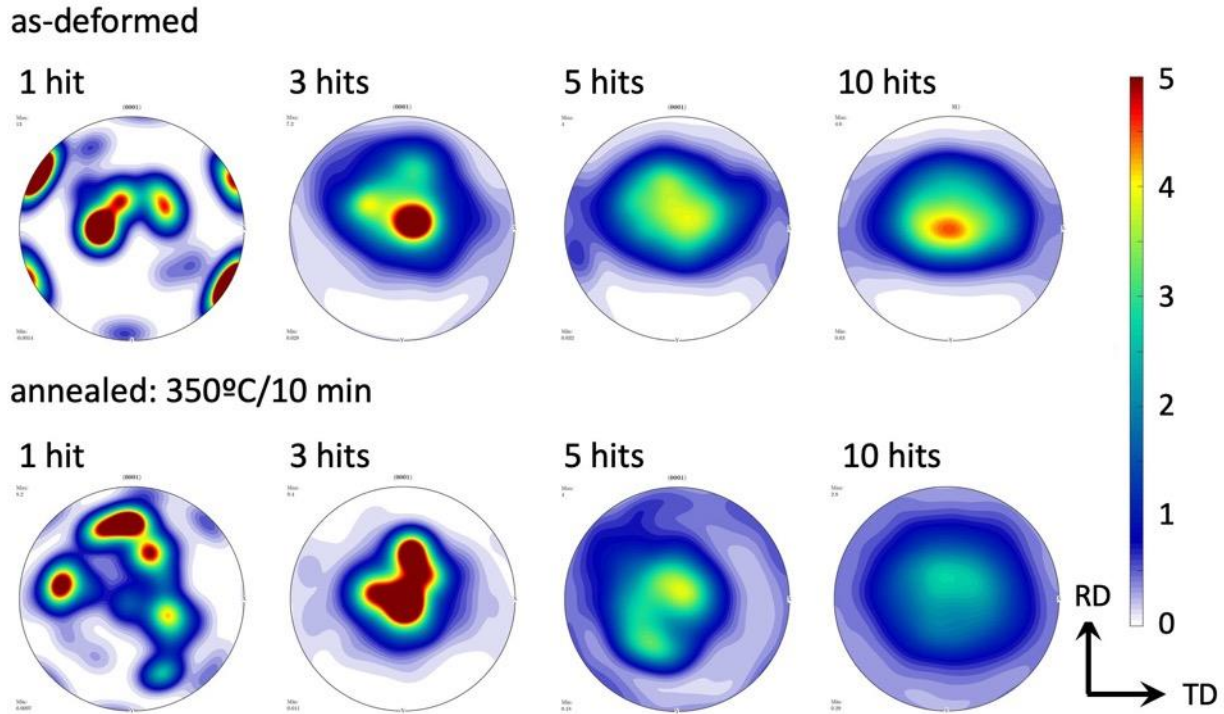


Figure 13: Pole Figures of ZX30 samples through the 10-pass process in the (top) as-deformed condition and (bottom) after annealing at 350°C for 10 minutes

In summary, both texture and grain size are reduced with an increasing number of passes at a strain of 0.2. Deformation promotes the nucleation of randomly oriented RX grains, which nucleate preferentially within twins and along grain boundaries. As the grain size is refined, twinning decreases, but RX grains continue to nucleate along the increasing grain boundary area. The randomly oriented RX grains grow slightly during annealing, which leads to a reduction of the basal-deformation texture as they occupy a larger fraction of the microstructure.

Effect of the intermediate annealing step:

In the alloy study, the weakest final textures were achieved in the samples with the lowest fraction recrystallized and the largest spread in grain misorientations. Slower recrystallization kinetics, in that case, achieved through solute drag, promote weaker recrystallization textures in Mg-Zn-Ca alloys. In this portion of the study, recrystallization was restricted by limiting the duration of the intermediate annealing step with the goal of accumulating grain misorientation until the final annealing step. Several variations in the TMP schedule were explored (refer to Table II for a summary of all processing routines).

The first TMP variation consisted of twenty compressive hits in the ZX30 alloy. The strain per hit increased from a few percent for the first several passes, up to 25% per hit for the last three passes resulting in a total compressive strain of approximately 2.4. A strain rate of 1 s⁻¹ was used for all passes. Between passes, the samples were held at 350°. The duration of this thermal soak, referred to as the intermediate anneal, was varied, with samples being allowed to anneal for

either 15 s or 300 s. One sample was subjected to each routine. After Gleeble testing, half of the sample was annealed in a box furnace at 350°C for 10 minutes.

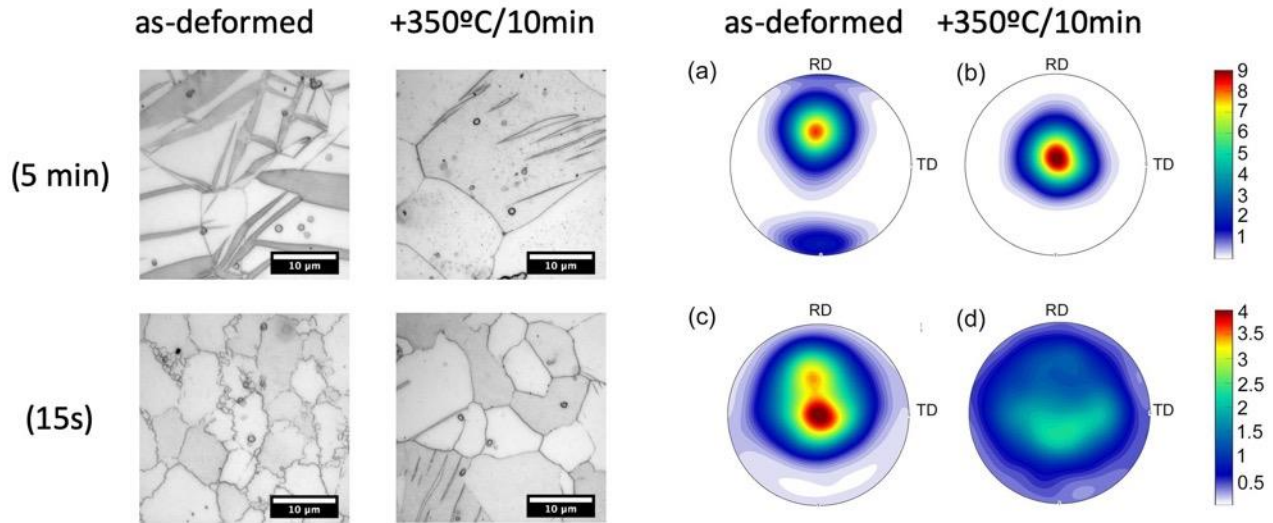


Figure 14: Optical microscopy images and basal pole figures of ZX30 after the 20-pass schedule with a 5 min intermediate annealing step (top row) and ZX30 after the 20-pass schedule with a 15s intermediate annealing step (bottom row).
Correction: Scale bar units should read 20 μm .

A comparison between the as-deformed and annealed samples is given in Figure 14. The 20-pass sample processed using the longer intermediate annealing exhibits profuse twinning in many regions of the deformed material. The 20-pass sample with the short 15s intermediate annealing treatment exhibits serrated grain boundaries and a necklace structure of small DRX grains along the boundaries of the larger grains. The as-deformed grain size is smaller when using the shorter intermediate anneal. The final annealing treatment resulted in equiaxed grains for both processing conditions, but the grain size remained finer in the 20-pass (15s) sample.

Consistent with the observations in the alloy study, the sample with evidence of DDRX and restricted grain boundary mobility also exhibits a weaker texture both before and after annealing (Figure 14). The 20-pass sample with the longer intermediate anneal has a significantly stronger basal texture that is largely unaffected by annealing, much like that seen in the dilute alloys. This demonstrates that both strong basal and weak TD-spread textures can also be produced in ZX30. Alloying and processing both control texture development.

If it is possible to decrease basal texture intensity by reducing the length of the intermediate anneal, that it seems reasonable that increasing the length of the intermediate anneal could allow for an increased amount of static RX between passes and an increased basal texture intensity. For this study ZX30 was subjected to the 10-pass schedule, but with an increased intermediate annealing duration of 30 minutes (10-pass (30min)). After Gleeble testing, half of the sample was annealed at 350°C for 30 minutes.

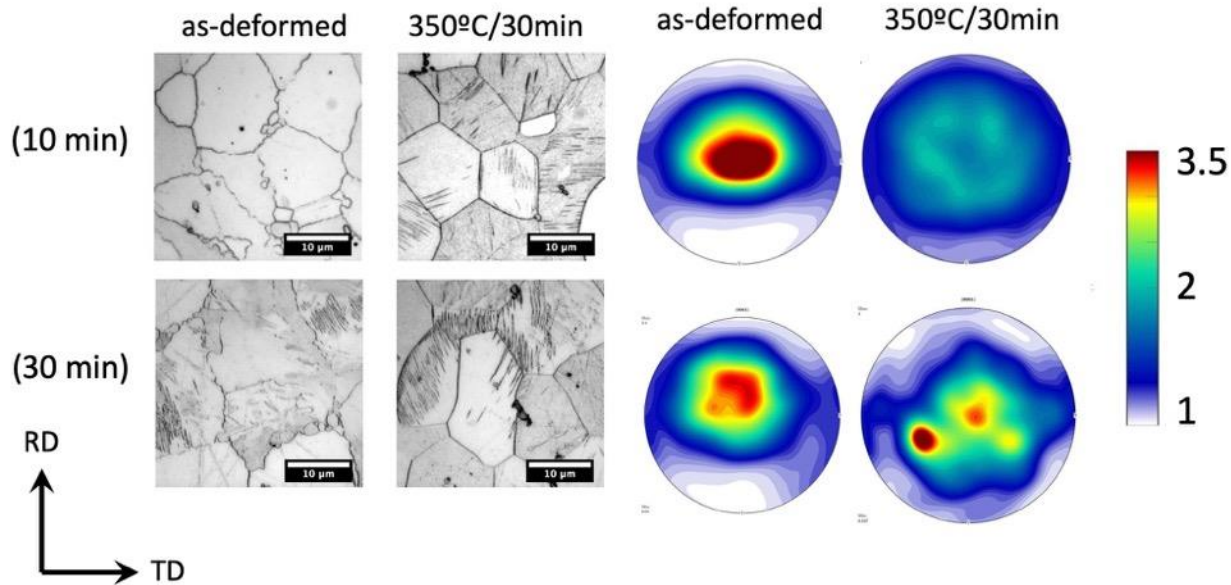


Figure 15: Optical microscopy images and basal pole figures of ZX30 after the 10-pass schedule with the standard 10 min intermediate annealing step (top row) and ZX30 after the 10-pass schedule with a 30 minute intermediate annealing step (bottom row). Correction: Scale bar units should read 20 μm .

The longer intermediate annealing treatment did lead to a stronger basal texture than the 10-minute intermediate anneal during processing (Figure 15), but still produced a relatively weak basal deformation texture (<5 MRD). The as-deformed microstructure still consists of serrated grain boundaries and some small DRX grains, suggesting that Zn and Ca solutes in ZX30 reduce recrystallization kinetic sufficiently even given the longer intermediate annealing time. The longer intermediate anneal did permit some grain growth and the increased grain size allowed for more twinning activity during deformation (not shown).

Some of the early work in this study on the ZX30 alloy also looked at the effect of the intermediate annealing time, but after only 5-passes and using a lower strain rate of 0.1s^{-1} [18]. As will be discussed in the next section, texture is strain rate dependent. For this processing routine, varying the duration of the intermediate annealing step between 2 minutes and 10 minutes was not found to significantly affect the final texture after a final 10-minute annealing treatment at 350°C . These final annealing treatment in these samples was performed in the Gleeble, so the as-deformed microstructure is unknown.

Effect of strain rate:

Strain rate is expected to affect both the dynamic and static recrystallization kinetics and therefore it will influence texture development in the Mg-Zn-Ca alloy system. Strain rate was varied from 0.1s^{-1} to 1s^{-1} in the ZX30 alloy, while keeping all other parameters fixed in the 10-pass TMP schedule. Post-deformation, a 10-minute annealing treatment at 350°C was applied in the Gleeble. These specimens were not studied in the as-deformed condition. A comparison of the basal texture after annealing is shown in Figure 16.

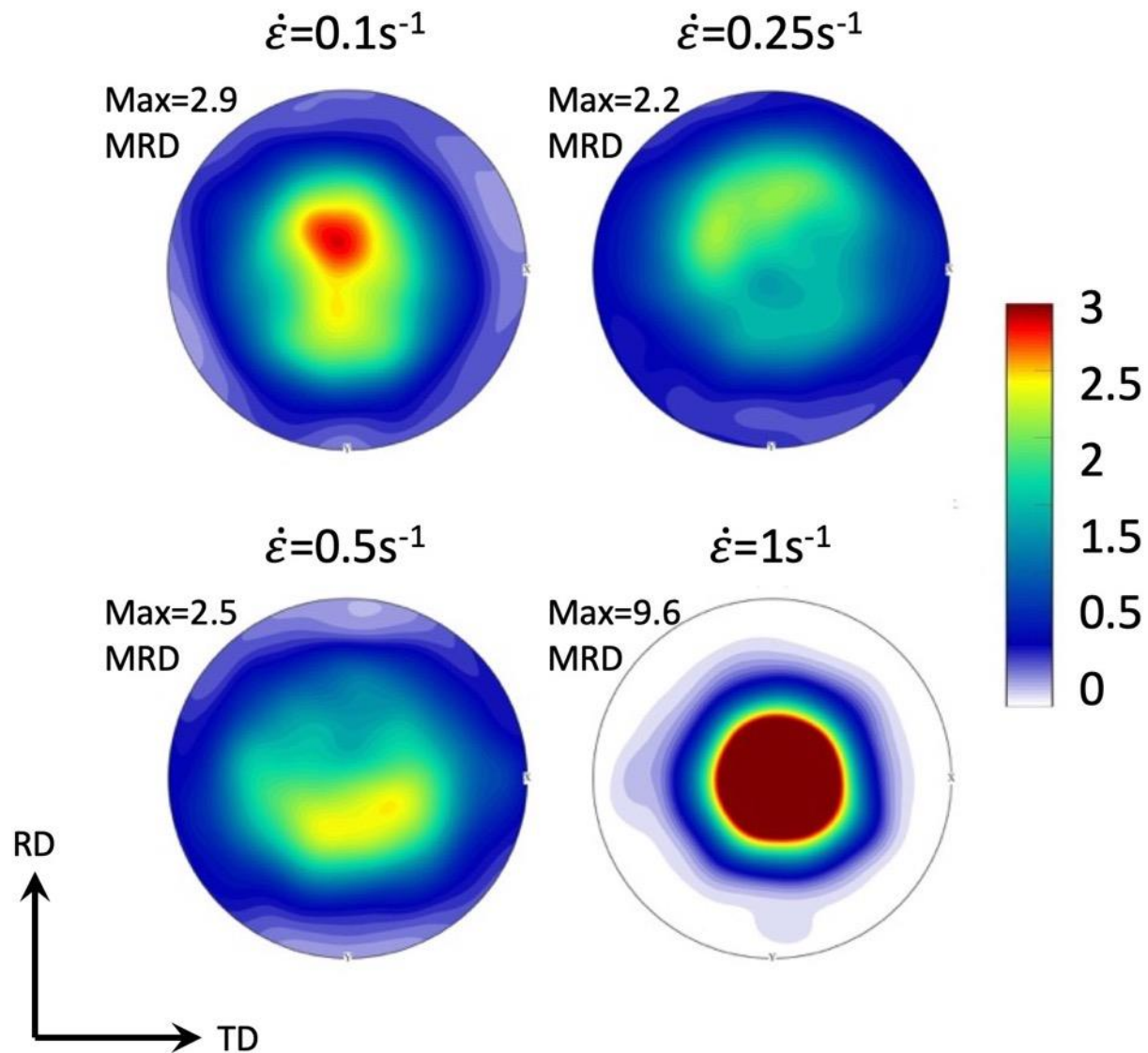


Figure 16: Basal pole figures of ZX30 samples subjected to the 10-pass schedule but with different strain rates. All samples were subjected to a final annealing treatment of 350°C for 10 minutes.

A strain rate of 1s^{-1} produced an undesirably strong basal texture in the ZX30 alloy with the 10-pass schedule. In some additional ZX30 samples, this high strain rate lead to strain localization and non-uniform deformation. For the specimen included in Figure 16, the microstructure was fairly uniform and consistently basal. The intermediate strain rates produced the weakest textures after annealing.

Static Recrystallization in 10-pass ZX30:

A final annealing treatment of 350°C for 30 minutes was shown to lead to a significant change in texture in the “10-pass” ZX30 (and ZX31) samples. It is of particular interest to perform the annealing treatment at a lower temperature, with slower kinetics, so that the microstructure and texture evolution can be captured early in the recrystallization process and also to develop a model to describe the kinetics of recrystallization at multiple temperatures. This information can be used to help determine the appropriate final annealing treatment and thermal soak between passes. Annealing treatments have been performed at both 300°C and 350°C for various durations on ZX30 subjected to the standard 10-pass process (10 min intermediate anneal). Optical microscopy and two methods of EBSD analysis were used to quantify the extent of recrystallization.

A microstructure consisting of primarily of equiaxed grains is likely fully recrystallized. Figure 17 demonstrates the microstructure evolution that occurs in the 10-pass ZX30 specimen during post-deformation annealing at 300°C and 350°C. At 300°C, with treatments less than 30 minutes, the grain boundaries are serrated and irregular and the microstructure consists of both small, likely RX grains, and larger irregular grains. The structure is more equiaxed for treatments 30 minutes and greater, though some irregular grains still exist at 30 minutes. At 350°C that transition to a more equiaxed structure occurs by 10 minutes. Based on optical microscopy alone, it appears that full RX occurs by 60 minutes at 300°C and 15 minutes at 350°C. This is used to guide the EBSD metrics for quantifying RX.

Grain Orientation Spread (GOS) is a measure of the misorientation between the average grain orientation and the orientation of each individual measurement point within a grain. In GOS maps the grains are assigned a color based on the average of these misorientations. This method of characterizing grain misorientation is grain size sensitive with smaller grains tending to have lower GOS values and therefore appearing to be more recrystallized. In this work, grains with a GOS \leq 1° are considered recrystallized. This is a commonly used cutoff and Figure 18(a) illustrates that in 10-pass ZX30 samples annealed at 350°C almost all the grain fall under the cutoff after 30 minutes.

Grain average misorientation (GAM) is a measure of the misorientation between an individual measurement point and its neighboring points within the grain. In GAM maps the grain are assigned a color based on the average of these nearest-neighbor misorientations. As nearest neighbor misorientation is more likely to increase with increasing step size in deformed grains, the method of characterizing RX is step size dependent. In the current work, grains with GAM less than 0.8° are considered RX for EBSD maps collected using a 1.2 μm step size. This cutoff was determined by looking at GAM histograms in samples that are expected to be fully RX, such as the 10-pass ZX30 samples annealed at 350°C for 30 minutes and 60 minutes as shown in Figure 18(b).

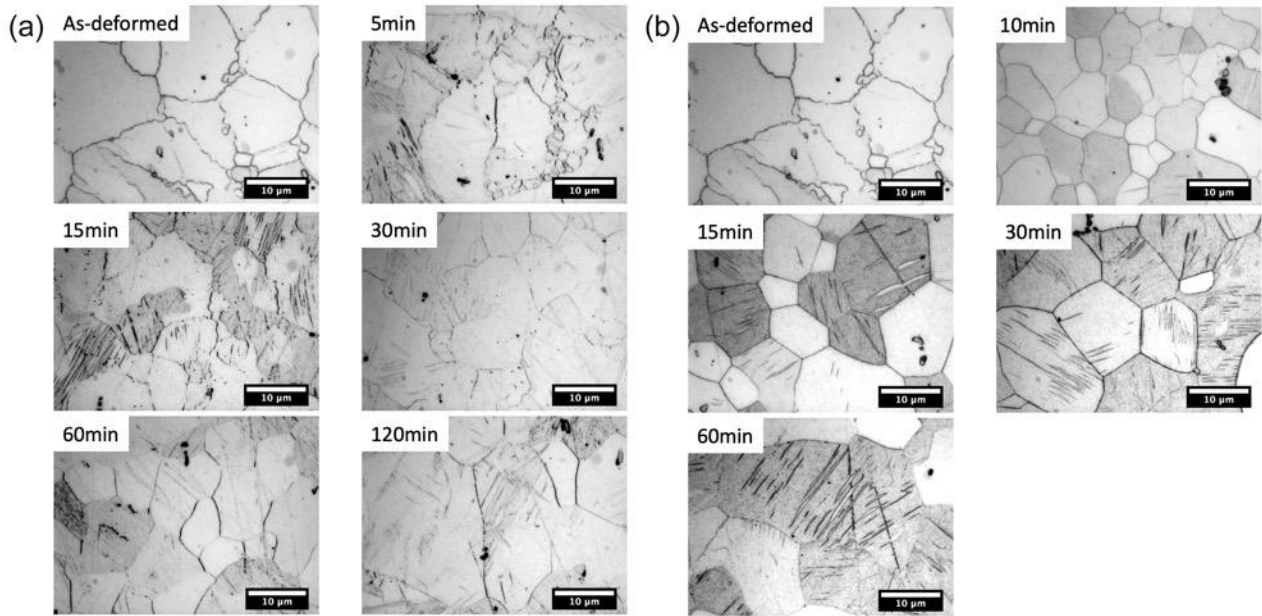


Figure 17: Optical micrographs of the ZX30 specimen subjected to the 10-pass TMP schedule after annealing for various times at (a) 300°C and (b) 350°C. Correction: Scale bar units should read 20 μm .

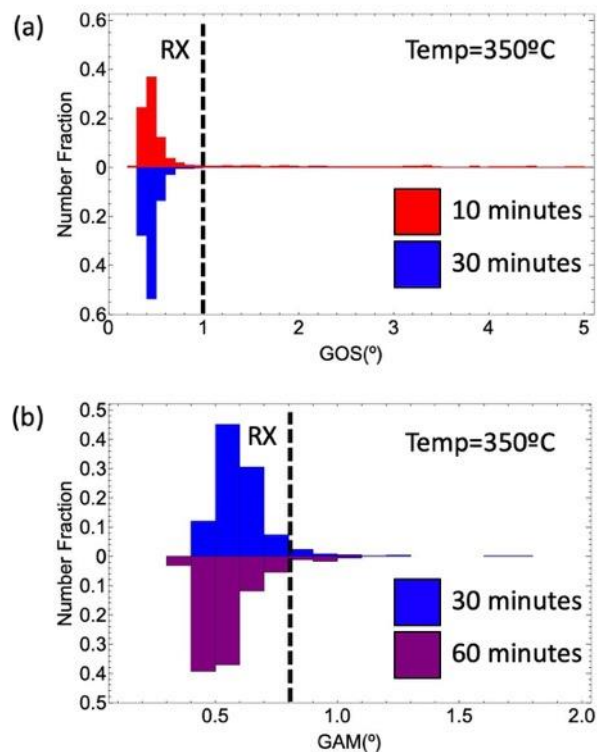


Figure 18: Histograms of (a) GOS and (b) GAM in 10-pass ZX30 samples annealed at 350°C illustrating the cutoffs used to distinguish between RX and deformed grains.

A summary of the % RX calculated using GOS during post-deformation annealing in the 10-pass ZX30 samples is shown in Figure 19. The solid lines are rough predictions based on a Johnson-Mehl-Avrami-Kolmogorov (JMAK) recrystallization model. The estimated fraction recrystallized at 60 minutes falls below the predictions at both temperatures. This is likely a consequence of grain growth as larger grains tend towards larger GOS values as optical microscopy suggests nearly complete RX after 60 minutes of annealing at both of these temperatures. In order to avoid grain growth complications, GAM analysis was applied to the same maps.

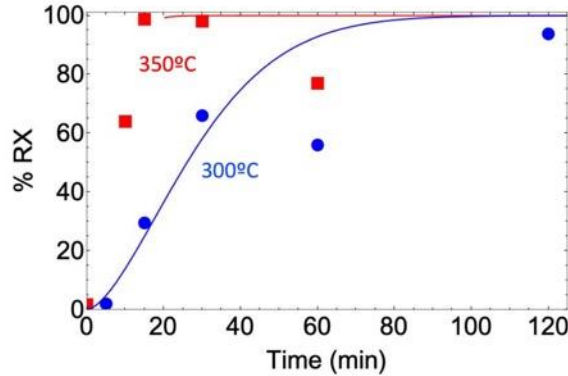


Figure 19: %RX in annealed 10-pass ZX30 samples calculated using GOS.

A comparison of the % RX in 10-pass ZX30 samples annealed at 300°C is shown in Figure 20. As GAM is step-size dependent, only EBSD scans collected with a 1.2μm step size are included in this comparison. The GAM method of characterization leads to an unreasonably high %RX in the as-deformed condition based on optical microscopy. However, GAM measurement indicates that complete (100%) recrystallization occurs after 60 minutes at 300C which is more consistent with the micrographs than the 50% RX that is calculated using GOS at the same time. Further analysis is needed before determining the most suitable EBSD step size and GAM cutoff, but 0.8° will be used for the remainder of this report.

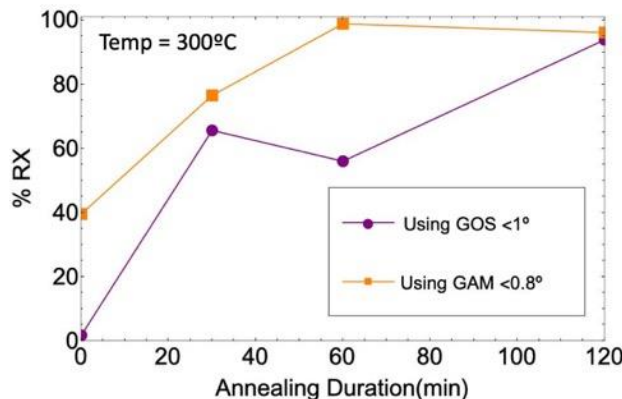


Figure 20: Plot of % RX in 10-pass ZX30 samples annealed at 300°C as determined using both GOS and GAM analysis of EBSD maps.

In addition to characterizing the fraction recrystallized, the EBSD maps also provide important information on the crystallographic texture. In addition to characterizing the grains as RX or deformed, the grains were also characterized as basal or non-basal, with basal grains being those with their c-axis tilted less than 40° from the sample normal and non-basal grains being those with a greater tilt. Figure 21 illustrates different ways to partition these grains by plotting circles on the standard HCP inverse pole figure. The diameter of the circle corresponds to the grain diameter. The color of the circle relates to its orientation, this information is redundant to its location on the IPF triangle. For example, red basal grains will always be found in the left corner which corresponds to the basal pole. Figure 21 specifically compares the 10-pass ZX30 in the as-deformed condition (left) and after a recrystallization annealing treatment (right).

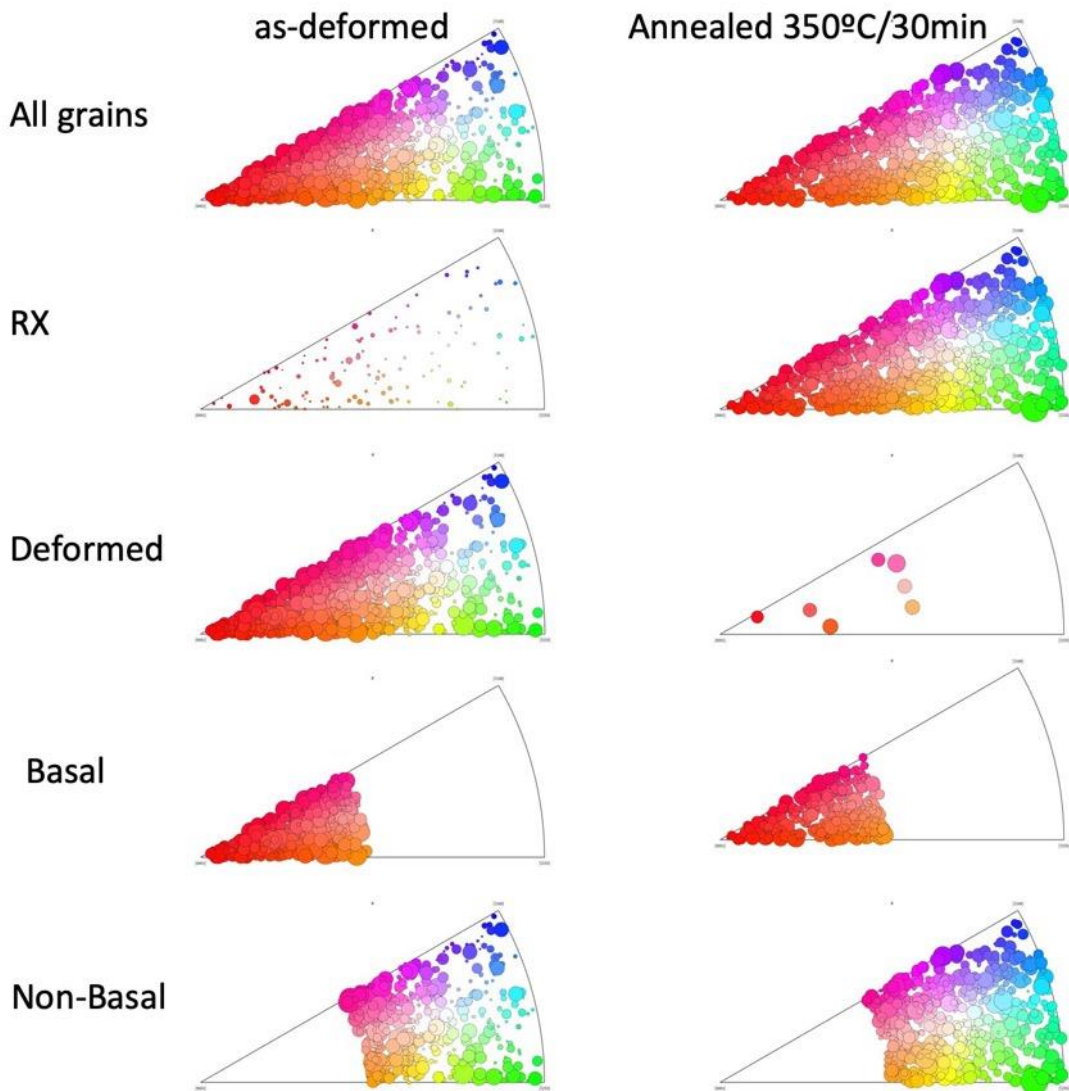


Figure 21: Inverse Pole Figures repetitive to the normal direction for 10-pass ZX30 samples in the (left) as-deformed condition and (right) after annealing at 350°C for 30 minutes. The size of the circle corresponds to the grain diameter. The color of the circle corresponds to the grain orientation (redundant information to it's location in the IPF triangle).

In both the as-deformed and annealed conditions, it is obvious that the RX grains (here using $<1^\circ$ GOS) are randomly oriented as they are distributed fairly evenly about the IPF triangle. During

annealing, the number and diameter of the RX grains increases, meaning that these randomly oriented grains occupy a larger fraction of the sample volume. There are very few deformed grains in the annealed condition and they tend to have a more basal orientation, though a few are outside the 40° basal/non-basal cutoff used in our further analysis. During RX the density non-basal grains decreases, while the density of basal grains increases.

A more quantitative analysis of how the area fraction of basal and non-basal grains evolves during annealing is presented in Figure 22. In a sample with a random texture, 20% of the grains would be expected to have a basal texture using the 40° cutoff. Over 50% of the deformed grains are basal. As annealing progresses, the deformed grains are consumed by the more randomly oriented basal grains. This leads to the decrease in basal texture intensity previously observed in the 10-pass ZX30 samples.

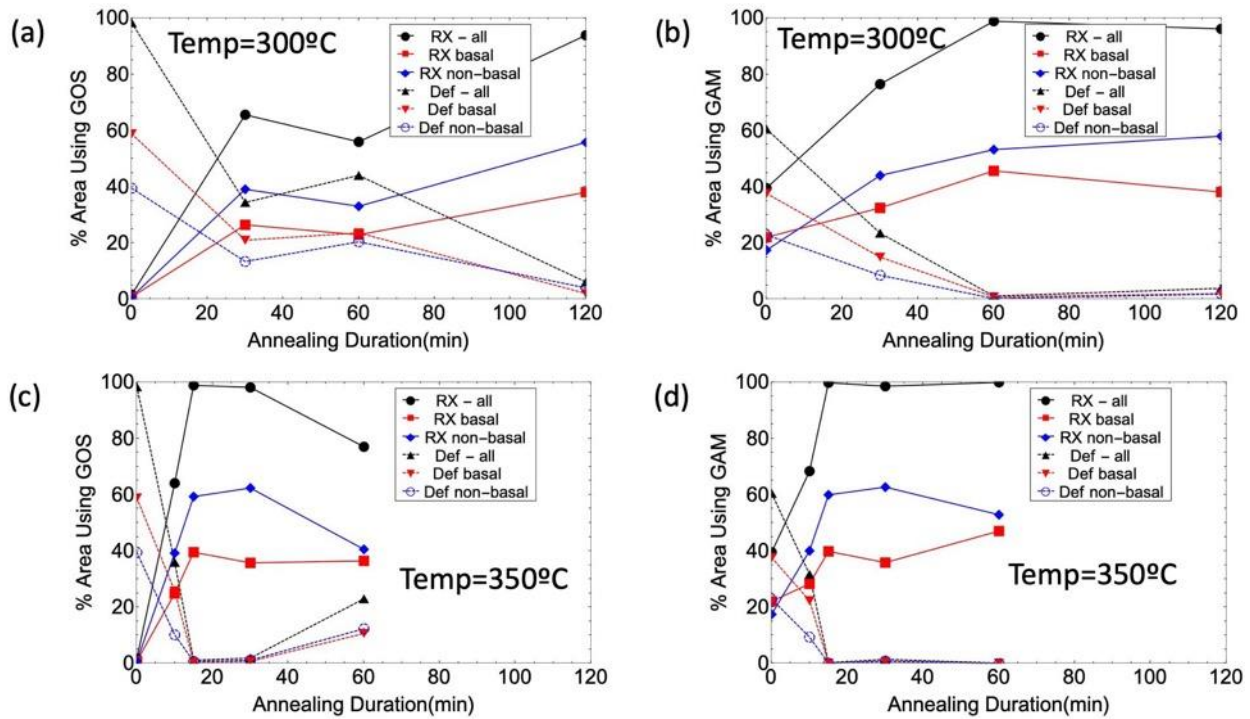


Figure 22: Plots showing the evolution in the area fraction of deformed and recrystallized grains at 300°C (top) and 350°C (bottom) using both the GOS (left) and GAM (right) methods of characterization.

In order to better observe the early stages of recrystallization, higher resolution EBSD scans were collected in the as-deformed condition and after 5 min, 15min, and 30 minutes at 300°C. Given the smaller area covered, and the inhomogeneity in the microstructure before full recrystallization, these scans should not be considered fully representative of the microstructure. IPF maps of these scans are shown in Figure 23. Little evolution is seen after 5 minutes at 300°C. After 15 minutes the smaller, more randomly oriented grains begin to dominate the microstructure. After 30 minutes the grain size is more uniform and the lack of color gradients and a decrease in the fraction of un-indexed white pixels demonstrates less misorientation within the grains, one marker of recrystallization.

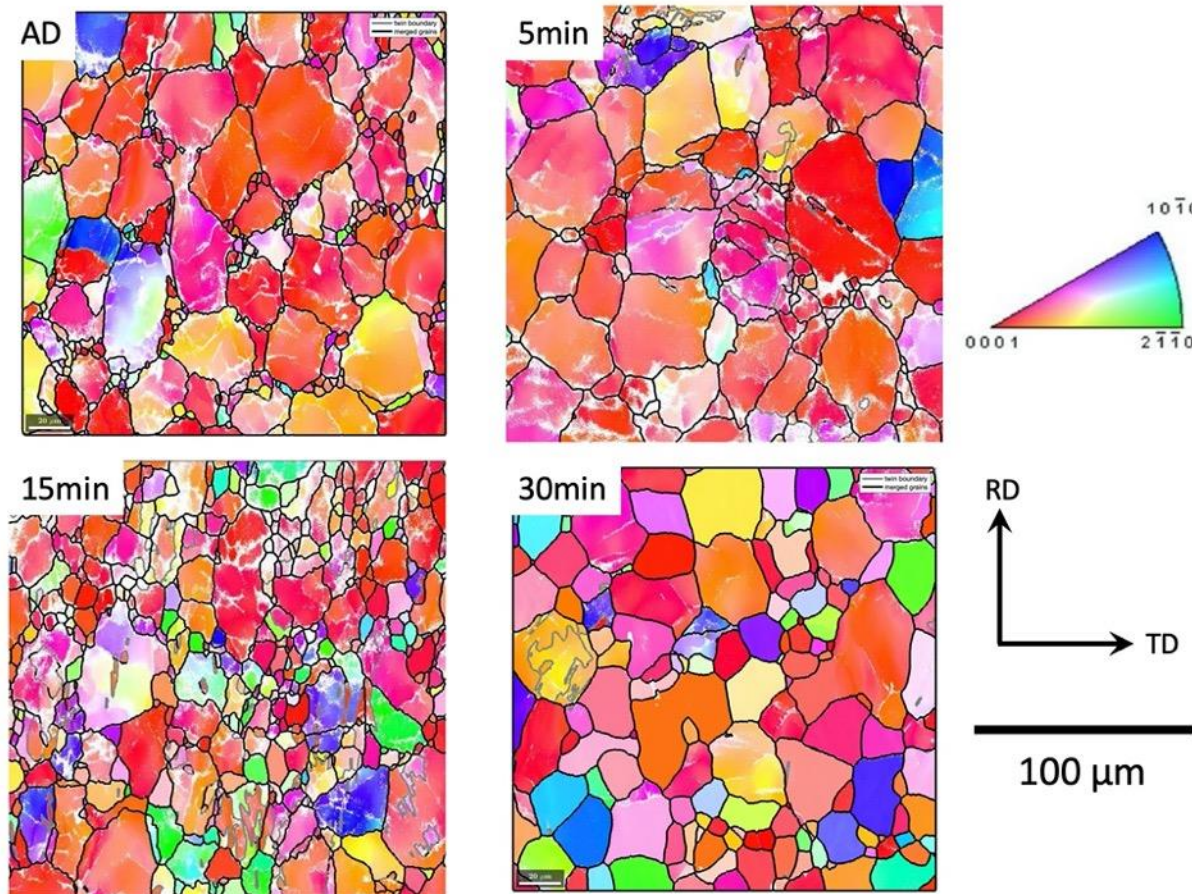


Figure 23: IPF maps of the higher resolution EBSD scans showing the evolution of microstructure in 10-pass ZX30 samples during annealing at 300°C.

In conventional Mg sheet texture is often unchanged, or becomes sharper during static annealing [19–21]. In contrast, the texture has been observed to weaken in Mg-Zn-(Ca,RE) and RE containing alloys [13,22,23]. One proposed mechanism for this reduction is that the solutes alter grain boundary energies and mobilities, which may reduce the bias which selects for basal oriented grains during static recrystallization [5,24,25]. This study supports findings that the nucleation and growth of randomly oriented RX grains leads to weaker basal textures in Mg-Zn-Ca alloys.

Process optimization in ZX21:

It was demonstrated earlier that the alloys with 3.2 wt% Zn (ZX30 and ZX31) had a weaker texture than the ZX21 alloy, however the TMP process used for the alloy comparison had been optimized using the ZX30 alloy. In ZX30 limiting recrystallization and grain growth between passes seems to be essential for producing a weak final texture, and therefore a reduced deformation temperature and a reduced intermediate anneal were explored for process optimization in ZX21. A ramped schedule, in which the strain per pass increases as the thickness (and grain size) is reduced, is often

utilized in rolling to reduce edge cracking, and therefore a ramped 12-pass schedule was also employed. In the ramped schedule, the strain was increased from 0.05 on the first pass to 0.25 for the last three passes, in addition the temperature was decreased from 350°C to 325°C for those final passes. A summary of the tests performed on ZX21 is shown in Table III. The sample tested at a lower temperature (300°C rather than 350°C) cracked during Gleeble testing and was not studied further (Figure 24).

Table III: Tests run on the ZX21 alloy

sample name	process name	# of passes	temp (°C)	strain per pass	duration of intermediate anneal (s)
D30	10-pass	10	350	0.2	600
Q02	10-pass - 15s	10	350	0.2	15
300D01	10-pass - 300C	10	300	0.2	600
5D06	10-pass - 5 min	10	350	0.2	300
RampD04	Ramp	12	350 to 325	0.05 to 0.25	300



Figure 24: Photograph of cracking in ZX21 sample subjected to 10-pass PSC testing at 300°C

EBSID IPF maps comparing the annealed (350°C/30min) microstructures of the 4 TMP schedules used on ZX21 are shown in Figure 25. Curiously, for the 10-pass schedule, the final grain size is larger with a 5min intermediate anneal than it is when using a 10 min or 15s intermediate anneal.

This may be a result of inhomogeneity in the original cast microstructure. The grain size observed using the Ramp schedule is comparable to that observed when using a 5-min intermediate anneal in the 10-pass schedule. The two larger grained ZX21 samples are not fully RX (using GOS) and show bands of higher GOS grains perpendicular to the rolling direction (Figure 26).

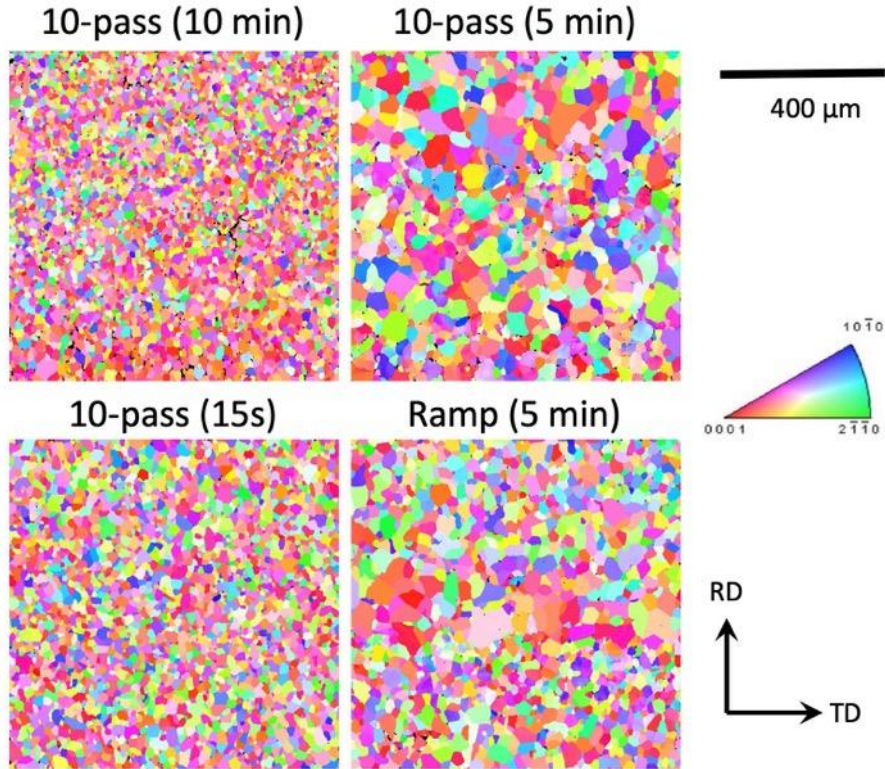


Figure 25: EBSD IPF maps of ZX21 samples comparing different processing routes after the final annealing step. The duration of the intermediate anneal is given in the parenthesis.

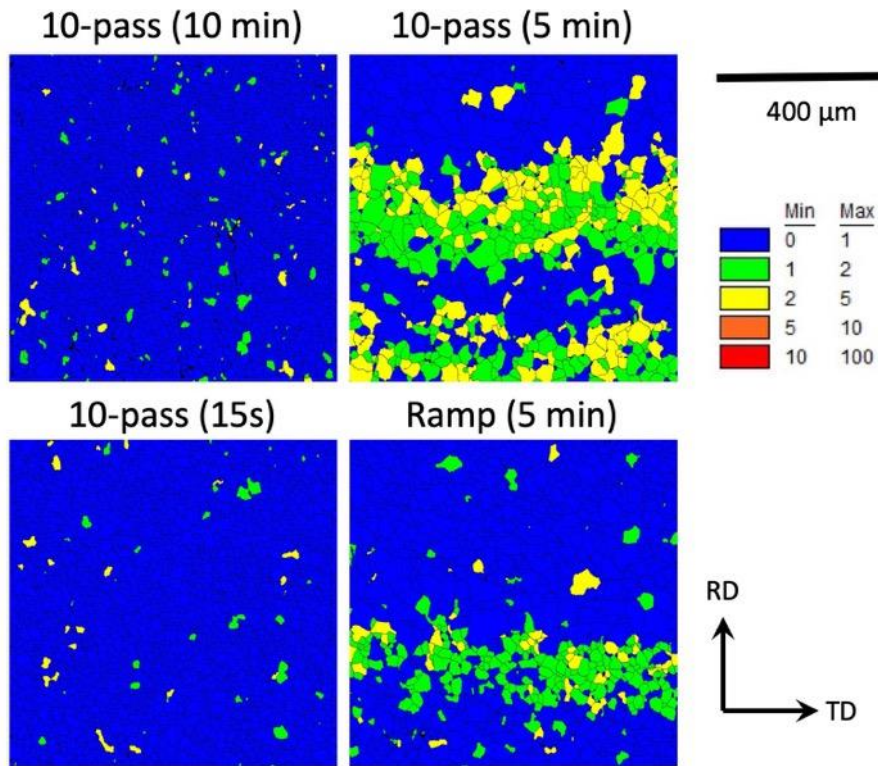


Figure 26: EBSD GOS maps of ZX21 samples comparing the extent of RX using different processing routes after the final annealing step.

As intended, shortening the duration of the intermediate annealing step did lead to a reduction in texture in all of the modified processing schedules (Figure 27). The texture in the annealed state is relatively weak after all four processing schedules. The texture is the strongest in the 10-pass schedule with the 10-minute intermediate annealing duration. Further texture weakening may occur in the sample with the 5-minute intermediate anneal and when using the ramp schedule if the duration of the final annealing treatment was increased to ensure complete static RX.

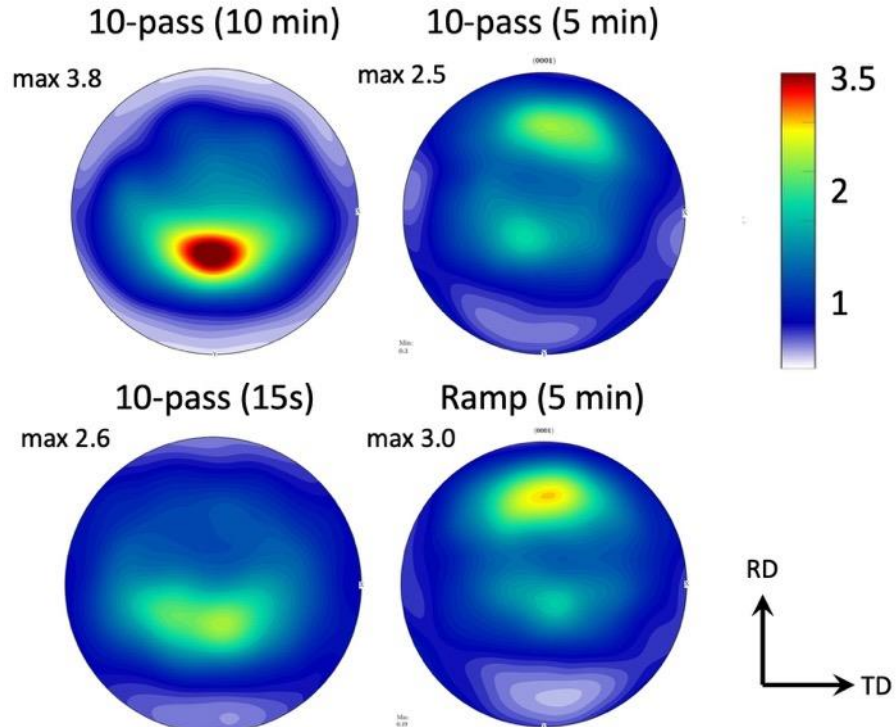


Figure 27: Basal pole figures of ZX21 samples comparing different processing routes after the final annealing step of 350°C for 30 minutes.

Texture and Formability in Mg sheet alloys studied in this project:

The formability and texture of several Mg alloy sheets was characterized in support of other tasks. As demonstrated in the Mg-Zn-Ca system, processing, not only alloying, plays a role in texture development. Differences in mechanical behavior were observed between the different batches of the E-Form Plus alloy (nominally Mg-2Al-1Zn-0.8C-0.3Mn) received during this project. Differences in texture, one of the key properties influencing formability and planar anisotropy, was found to be the primary source of the variability.

Basal pole figures for the four different batches of EFP are shown in Figure 28. Although the maximum intensity in the basal pole figures are all quite low for Mg alloy sheets (3 or less MRD), there are significant differences in the distribution of the intensity. Based on texture alone, Batch 1 would be expected to be the most formable as it has the lowest texture intensity and the c-axis of the majority of the grains is tipped down away from the sample normal, allowing for activation of basal slip in through thickness deformation. The “quad” texture in Batch 1 consists of split intensity peaks in both the RD and TD. Batch 2 has only a single peak in the center of the basal pole figure, meaning the majority of grains in the sheet are oriented such that their c-axis is aligned with the sheet normal. This undesirable texture was demonstrated to result in poor formability but does result in decreased planar asymmetry. The texture in Batch 3 exhibits basal peak splitting in only the TD, a texture that allows for easier activation of basal slip with through thickness deformation, but results in asymmetry within the plane of the sheet. The Batch 4 material exhibits

a texture between that of Batch 1 and Batch 3, but more similar to Batch 3 with respect to the intensity of the TD-split peaks.

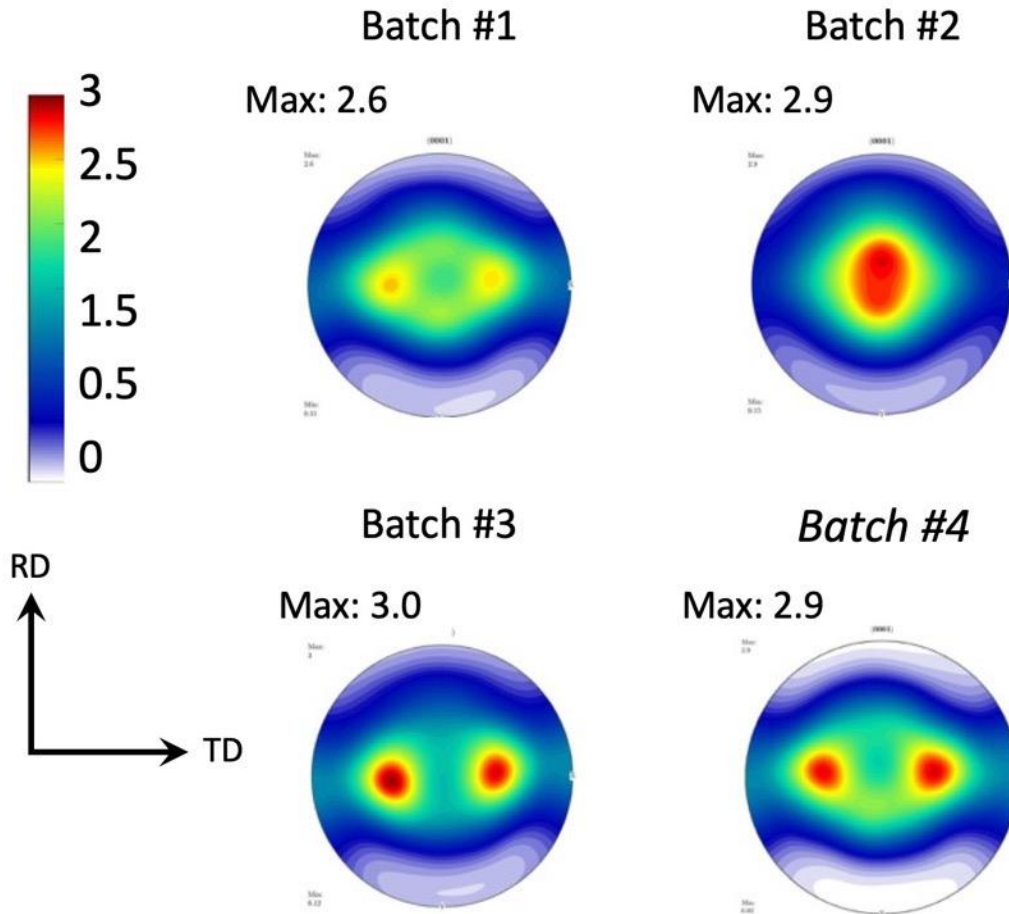


Figure 28: Basal pole figures describing the texture in the four different batches of EFP used in this project.

Room temperature dome height (Erichsen cup) testing:

Erichsen cupping tests were conducted at room temperature using a sheet clamping force of 10 kN, a deformation rate of ~5.6mm/min, and using graphite lubrication on the tool. Tests were concluded when cracking was visually observed, which also correlates to a drop in the force-displacement curve. The Erichsen dome height was calculated as the displacement at which the force dropped. In addition to ZEK100 and EFP sheet (summarized in Table IV), various samples of Alloy 2 and Alloy 2+ were studied as well.

Table IV: Summary of Erichsen dome height tests in ZEK100 and EFP

Alloy	Mean Erichsen Dome Height (mm)	Standard Deviation (mm)	Crack Orientation
ZEK100	6.7	0.1	all parallel to TD
EFP Batch 1	6.2	0.6	No strong preference in orientation
EFP Batch 2	4.6	0.4	all parallel to RD
EFP Batch 3	6.5	0.4	all parallel to RD

Elevated temperature deep draw testing:

Elevated temperature deep draw tests were conducted on the ZEK100 (1.6 mm thick), E-Form Plus (EFP) Batch 1 (1.2 mm thick), and EFP Batch 3 sheets. Due to the low draw heights achieved at 100°C, room temperature tests were not conducted. Circular blanks 65mm in diameter were punched from the sheets. Tests were conducted with an Erichsen Universal Sheet Metal Testing Machine Model 142-40 with a 32mm outer diameter punch. This work used a blank holding force of 10 kN and a punch displacement rate of ~ 6mm/min (lower than used for the forming tasks). For the deep draw test, the blank, die, and tooling (aside from the punch) are heated externally to the desired temperature. Once the desired temperature is reached, the assembly was held at that temperature for 10 minutes at which point it was transferred into the sheet formability machine and the test was initiated as quickly as possible. No lubrication was used. Tests were terminated when the load dropped due to the formation of a crack or unusual force/displacement behavior was observed. At least three repeats were done for each condition. The results are summarized in Table V. The average draw refers to the total sheet displacement, not the displacement of the punch.

Table V: Results from deep draw testing in E-Form Plus and ZEK100

Alloy	Temperature (°C)	Ave. Draw (mm)	Standard Deviation (mm)
EFP – Batch 1	100	8.3	0.5
	200	15.2	1.9
	250	21	7.8
EFP – Batch 3	200	24.6	7.6
ZEK100	100	8.9	1.0
	250	11.0	0.5

The full draw (30 mm) was almost achieved in some of the EPF Batch 2 specimens at 200°C and in the EFP Batch 1 specimens at 250°C, but sample to sample variation was high in these materials. The maximum draw height before cracking at 100°C in EFP Batch 1 was significantly less (8.3 mm). At the higher temperature, ZEK100 exhibited less deep drawability than the EFP Batch 1 (11 mm) but the draw depths at 100°C were comparable. Representative comparisons of the cups at the different temperatures used are shown in Figure 29. For the low formability conditions, failure occurred near the location of the maximum bending radius. In several of the high temperature EFP tests, no cracks formed; the tests were terminated when the force-displacement curve showed hardening behavior which suggested the edges of the sheet would eventually fracture. This was done to limit debris in the sheet testing machine.

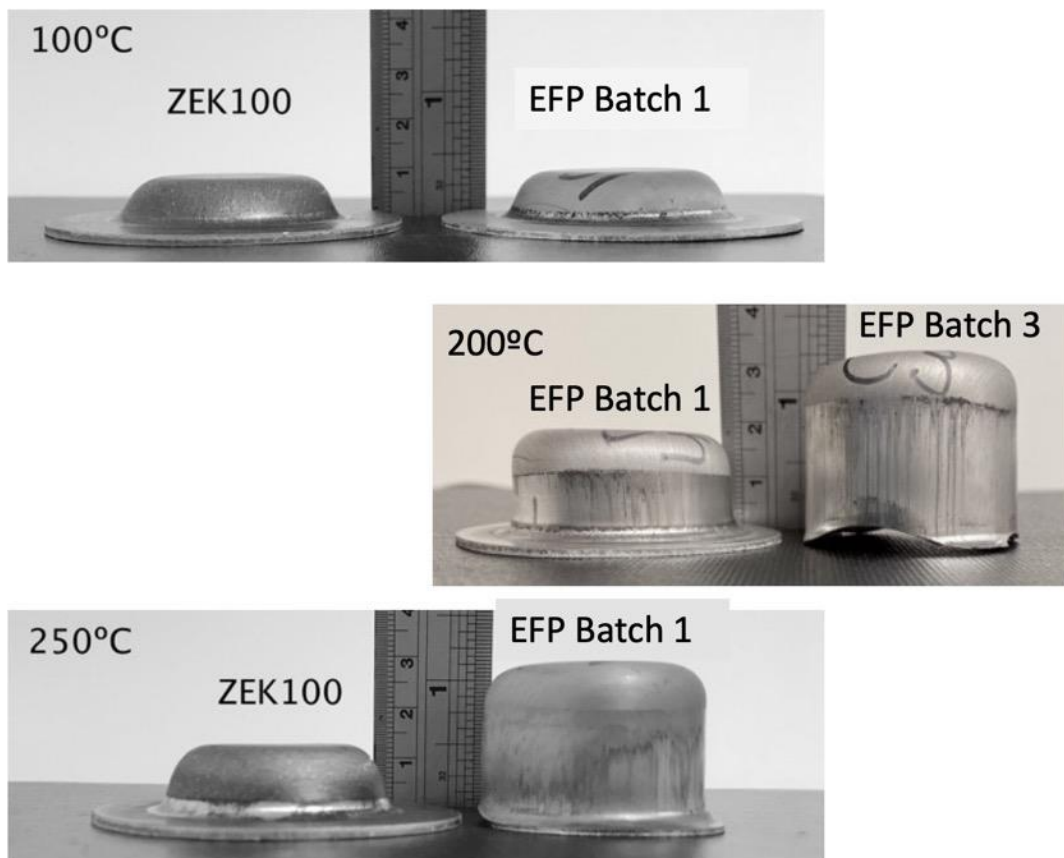


Figure 29: Comparison of deep draw cups at various temperatures.

Figure 30 shows the force-displacement curves for the different conditions. Here displacement refers to the punch itself; contact with the sheet was not made until a displacement of approximately 11mm. The ZEK100 requires more force to deform than the EFP Batch 1 at the same temperature. As expected, both alloys are softer at the higher temperature. The two batches of EFP show very similar force-displacement behavior at 200°C.

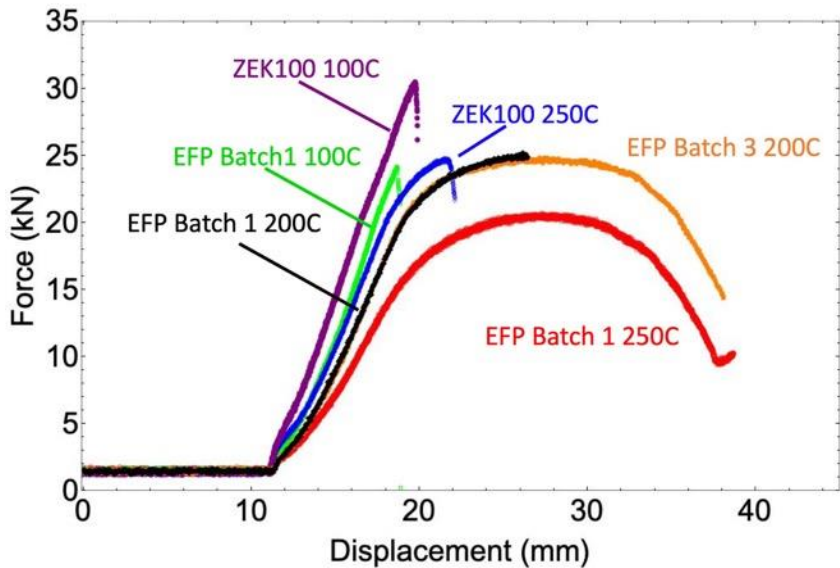


Figure 30: Representative force-displacement curves for the different deep draw testing conditions. Here displacement refers to the displacement of the punch.

Characterization of Alloy 2 Sheet Prepared by POSCO:

U of M received 2.5 sheets of as-rolled Alloy 2 produced by POSCO. Visual inspection of these sheets revealed some regions with cracking (Figure 31). The surface exhibited multiple features that appeared to be inclusions, but are likely marks from the sheet sticking to the rolls. Optical and scanning electron microscopy of the sheets revealed a high density of particles in strings elongated along the rolling direction (Figure 32).

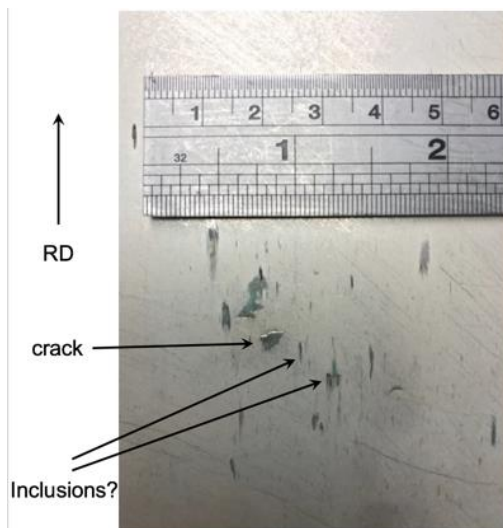


Figure 31: Surface defects on as-received Alloy 2 sheet

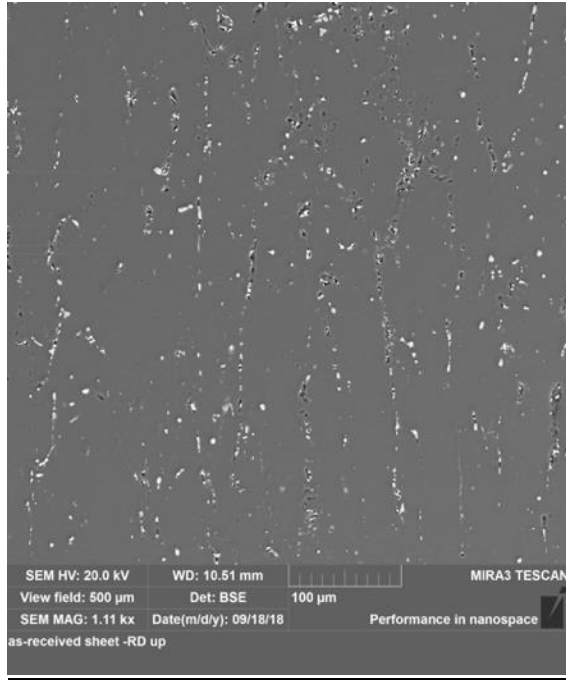


Figure 32: SEM image of as-received sheet. RD is vertical.

Several different annealing treatments were applied to coupons of the above Alloy 2 sheet following recommendations from Ohio State University and POSCO. The duration of the annealing treatment reflects the time at temperature. Annealed sheets were not quenched. It was found that all of the annealing treatments resulted in a similar final grain size, fraction of recrystallized grains, and texture (Figure 33). The as-rolled sheet did not have indexable patterns, likely due to the amount of residual deformation; this implies that very little dynamic recrystallization occurred during rolling. Thirty minutes at 350°C was selected as the annealing treatment to be used prior to formability testing given that it is further below the solidus (some incipient melting may occur at 400°C) and the duration is appropriate for industry.

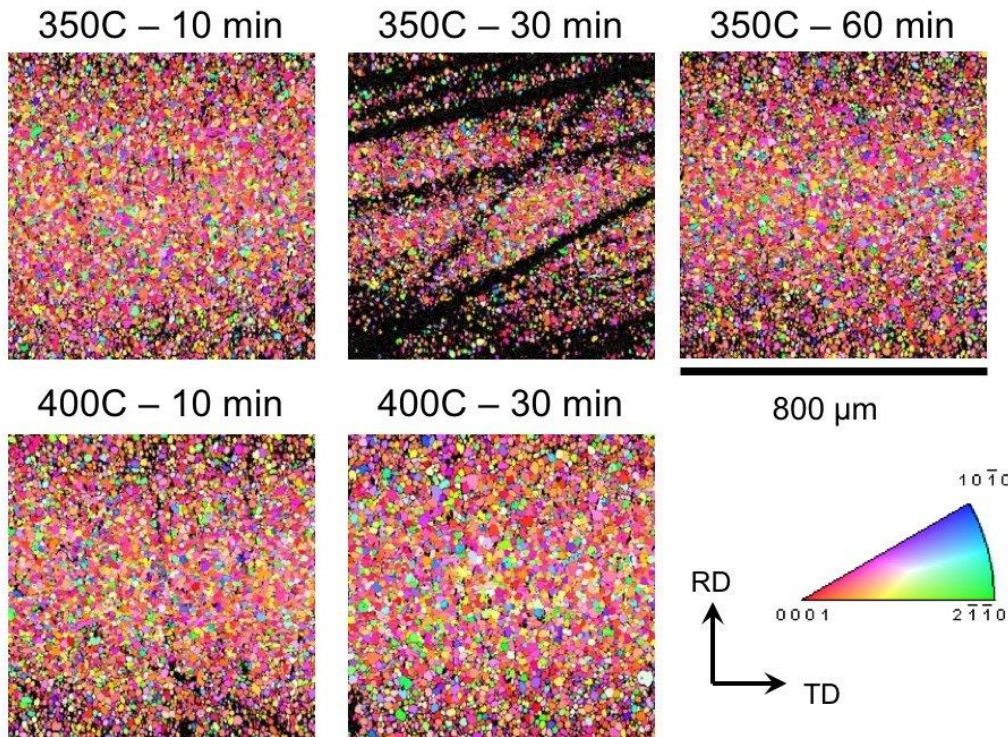


Figure 33: EBSD inverse pole figure maps of Alloy 2 after various annealing treatments

The texture observed in the annealed Alloy 2 sheets is comparable to that observed in the previously studied ZEK100 and EForm Plus sheets; a weak basal texture with an intensity around 3 MRD and a split in the transverse direction. This suggests that Alloy 2 will exhibit a similar formability to ZEK100 and EForm Plus provided the observed surface cracks and particle stringers are not detrimental to formability. Formability in these sheets was not tested at the University of Michigan.

Conclusions:

Desirable spread basal textures with a low texture intensity were produced in Mg-Zn-Ca sheet alloys through a combination of a 10-pass deformation schedule and a final recrystallization annealing treatment. For the selected processing conditions, Ca contents of at least 0.1 wt percent are required to produce the desired textures and Zn content strongly affected the texture in the as-deformed and annealed conditions. The three higher Zn ternary Mg-Zn-Ca alloys (ZX21, ZX30, and ZX31) showed a significantly reduced basal texture intensity in the as-deformed condition (max ~ 4 MRD) compared to the unalloyed and Mg-Ca binaries and the low Zn ternary (ZX0p50) (max intensities > 12 MRD). Annealing for 30 minutes at 350°C did not alter the strong texture in the dilute alloys or ZX0p50, nor did static recrystallization appreciably change the as-deformed texture in the ZX21 alloy. Significant basal texture evolution was observed during static recrystallization in the ZX30 and ZX31 alloys. The final weak texture of these two alloys exhibited a desirable annular structure, with the c-axis tipped from the normal

direction which is a desirable texture for improved formability. Increasing the Ca content from 0.1 to 0.3wt% did not lead to any appreciable differences in texture but did lead to an increase in secondary phase particles.

Microstructural signatures of discontinuous dynamic recrystallization, such as grain boundary bulging and serrated grain boundaries, were only present in the materials with weak textures in the as-deformed condition. The microstructure after 10-passes in these materials consisted of a necklace structure of small recrystallized grains surrounding larger deformed grains. The Mg-3.2Zn-Ca alloys have a lower fraction of recrystallization after ten deformation steps than the materials with stronger textures. The large spread in grain misorientations seen in the high Zn ternary alloys suggest limited recrystallization occurred throughout the ten deformation passes.

While the high Zn ternary alloys show promisingly weak textures, it is important to note that improper processing can lead to strong basal textures in these “good” alloys as well. Increasing the strain rate from 0.5s^{-1} to 1s^{-1} lead to a much stronger basal texture in the 10-pass ZX30. A longer intermediate annealing step lead to increased basal texture intensities as well.

Limiting static RX and grain growth until the final annealing treatment is essential to producing a weak texture. A high strain rate increases SRX kinetics allowing for increased recrystallization during the intermediate annealing passes. A longer intermediate annealing treatment allows for recrystallization and potentially grain growth to occur. Though not explored in this work, but based on the JMAK model, it is expected that decreasing the temperature of the intermediate anneal or increasing the temperature during deformation would also be an effective way to limit SRX between passes. Alloying is expected to influence the SRX and grain growth kinetics as well. In the most solute-rich ternary alloys, grain boundary mobility was limited by solute drag leading to restricted SRX and grain growth, and therefore weaker textures.

While limiting SRX during processing lead to improved textures, processing needs to promote DRX. This work demonstrates that the small, likely DRX grain have random orientations and that they exist through processing from the original deformation pass to the last. In order to optimize texture, it is important to control their nucleation and growth.

In contrast to the RX grains, the deformed grains tend to have a more basal orientation. During annealing, the volume fraction of the deformed grains decreases, leading to the decrease in basal texture intensity observed in the Mg-3.2Zn-Ca alloys. A basal deformation texture in magnesium alloys is not surprising due to the predominance of basal slip caused by the hcp crystal structure. What is interesting in the Mg-Zn-Ca system is that annealing leads to texture reduction rather than proliferation of the basal texture due to modified recrystallization kinetics [17].

This work consisted of a systematic study of how both alloying and processing influence texture in Mg-Zn-Ca ternary alloys and resulted in the creation of a large database linking processing with microstructure and texture. This database will serve as a foundation for establishing models for static and dynamic recrystallization kinetics, allowing for the development of ICME model to predict texture evolution throughout the rolling process.

References:

- [1] Y. Chino, T. Ueda, Y. Otomatsu, K. Sassa, X. Huang, K. Suzuki, M. Mabuchi, Mater. Trans. 52 (2011) 1477–1482.
- [2] B.C. Suh, J.H. Kim, J.H. Bae, J.H. Hwang, M.S. Shim, N.J. Kim, Acta Mater. 124 (2017) 268–279.
- [3] D.W. Kim, B.C. Suh, M.S. Shim, J.H. Bae, D.H. Kim, N.J. Kim, Metall. Mater. Trans. A Phys. Metall. Mater. Sci. 44 (2013) 2950–2961.
- [4] J.Y. Lee, Y.S. Yun, B.C. Suh, N.J. Kim, W.T. Kim, D.H. Kim, J. Alloys Compd. 589 (2014) 240–246.
- [5] D. Guan, X. Liu, J. Gao, L. Ma, B.P. Wynne, W.M. Rainforth, Sci. Rep. 9 (2019) 7152.
- [6] J. Luo, H. Yan, N. Zheng, R.S. Chen, Acta Metall. Sin. (English Lett.) 29 (2016) 205–216.
- [7] J. Bohlen, J. Wendt, M. Nienaber, K.U. Kainer, L. Stutz, D. Letzig, Mater. Charact. 101 (2015) 144–152.
- [8] J. Bohlen, J. Wendt, M. Nienaber, K.U. Kainer, L. Stutz, D. Letzig, Mater. Charact. 101 (2015) 144–152.
- [9] F. Bachmann, R. Hielscher, H. Schaeben, Solid State Phenom. 160 (2010) 63–68.
- [10] F.J. Humphreys, M. Hatherly, Recrystallization and Related Annealing Phenomena, 2nd ed., Elsevier, Netherlands, 2004.
- [11] T.D. Berman, T.M. Pollock, J.W. Jones, Metall. Mater. Trans. A Phys. Metall. Mater. Sci. 47 (2016).
- [12] A.D. Murphy, J.E. Allison, Metall. Mater. Trans. A Phys. Metall. Mater. Sci. 49 (2018) 1492–1508.
- [13] J. Bohlen, M.R. Nurnberg, J.W. Senn, D. Letzig, S.R. Agnew, Acta Mater. 55 (2007) 2101–2112.
- [14] M.T. Pérez-Prado, J. Bohlen, S. Yi, D. Letzig, T. Al-Samman, J. Robson, M. Barnett, W. Poole, C. Mendis, S. Agnew, N. Stanford, Jom 72 (2020) 2561–2567.
- [15] J.Y. Lee, Y.S. Yun, W.T. Kim, D.H. Kim, Met. Mater. Int. 20 (2014) 885–891.
- [16] C. Ha, J. Bohlen, S. Yi, X. Zhou, H.G. Brokmeier, N. Schell, D. Letzig, K.U. Kainer, Mater. Sci. Eng. A 761 (2019) 138053.
- [17] Z.R. Zeng, Y.M. Zhu, S.W. Xu, M.Z. Bian, C.H.J. Davies, N. Birbilis, J.F. Nie, Acta Mater. 105 (2016) 479–494.
- [18] T.D. Berman, J.E. Allison, in: Magnes. Technol. 2020, 2020, pp. 175–180.
- [19] J.J. Bhattacharyya, S.R. Agnew, G. Muralidharan, Acta Mater. 86 (2015) 80–94.
- [20] S.R. Agnew, O. Duygulu, Int. J. Plast. 21 (2005) 1161–1193.
- [21] M. a. Steiner, J.J. Bhattacharyya, S.R. Agnew, Acta Mater. 95 (2015) 443–455.
- [22] K. Hantsche, J. Bohlen, J. Wendt, K.U. Kainer, S.B. Yi, D. Letzig, Scr. Mater. 63 (2010) 725–730.
- [23] J. Victoria-Hernández, S. Yi, D. Klaumünzer, D. Letzig, Mater. Sci. Eng. A 761 (2019) 138054.
- [24] A. Imandoust, C.D. Barrett, T. Al-Samman, M.A. Tschopp, E. Essadiqi, N. Hort, H. El Kadiri, Metall. Mater. Trans. A Phys. Metall. Mater. Sci. 49 (2018) 1809–1829.
- [25] Z.R. Zeng, M.Z. Bian, S.W. Xu, C.H.J. Davies, N. Birbilis, J.F. Nie, Mater. Sci. Eng. A 674 (2016) 459–471.

Appendix I: Data availability

The experimental data generated during this project will be available by May 1st, 2021 on the Materials Commons at <http://doi.org/10.13011/m3-nsk8-kp39>.

The screenshot shows a dataset page on the Materials Commons platform. At the top, there is a navigation bar with the path: Projects / USAMP / Task 2 / Subtask 2.1 & 2.2 / UM / Experimental Data. Below the path, the dataset title is "Dataset: Dynamic recrystallization, texture, and grain growth + texture and formability" with a camera and eye icon. To the right of the title are two buttons: "Cancel review process" and "Edit". A note below the title states: "Electron backscatter diffraction (EBSD) was used to study the texture and microstructure unalloyed Mg, Mg-Ca binaries, and Mg-Zn-Ca ternary alloys subjected to plane strain compression. Also studied were the texture, microstructure, and formability (as measured using room temperature Erichsen cup tests and elevated temperature deep draw cupping tests) of ZEK100, EFP, alloy 1, and alloy 2 sheets from various sources." Another note below says: "Note: There was an error in the scale bar calibration for the optical images. All scale bars need to be multiplied by a factor of two (i.e. if it reads 100µm, the correct length is 200 µm)." At the bottom of the page, there is a file list with tabs for "Files", "Metadata", and "Activity Stream". The "Files" tab is selected, showing five files: "usamp-low-cost-mg-sheet-component-development-and-demonstration-pro ...", "Documentation.zip", "Sheet Formability Testing.zip", "Texture.zip", and "Gleeble.zip". Each file has a download icon and a dropdown menu icon.

File	Actions
usamp-low-cost-mg-sheet-component-development-and-demonstration-pro ...	Download ⚙️
Documentation.zip	Download ⚙️
Sheet Formability Testing.zip	Download ⚙️
Texture.zip	Download ⚙️
Gleeble.zip	Download ⚙️

EBSO_12_(USAMP_ZX30D19, USAMP_ZX30D21, USAMP_ZX30D29).zip	⚙️
EBSO_13_(USAMP_ZX30_D38.zip	⚙️
EBSO_14_(USAMP_ZX30D16, USAMP_ZX30D18, USAMP_ZX30D19).zip	⚙️
EBSO_15_(USAMP_ZX30_5D01, USAMP_ZX30D18,USAMP_ZX30D19.zip	⚙️
EBSO_16_(USAMP_ZX30_1D02).zip	⚙️
EBSO_17_(USAMP_ZX30_1D02, USAMP_ZX30_3D01.zip	⚙️
EBSO_18_(USAMP_ZX21_Q02,USAMP_ZX21_Ramp,USAMP_ZX21D).zip	⚙️
EBSO_19_(USAMP_ZX00_D31).zip	⚙️
EBSO_20_(USAMP_PureD34, USAMP_Pure01).zip	⚙️
EBSO_21_(USAMP_Pure01,USAMP_Pure02).zip	⚙️
EBSO_27_(A1).zip	⚙️
EBSO_23_(Alloy1,Alloy2,Eform_batch1).zip	⚙️
EBSO_25_(Eform_batch3,Eform_plane_scan).zip	⚙️
EBSO_24_(Eform_batch2).zip	⚙️
EBSO_26_(Eform_sheet).zip	⚙️
EBSO_28_(A2).zip	⚙️
USAMP Ingot Compositions.xlsx	⚙️
USAMP_ETL_Master_Global.xlsx	⚙️
EBSO_22_(USAMP_EFP4_2, USAMP_M12_4).zip	⚙️

Optical.zip	
EBSD_01_(ZX01_D33).zip	
SEM.zip	
EBSD_02_(ZX21_D33).zip	
EBSD_03_(ZX0p50).zip	
EBSD_04_(USAMPd17, Zek100, ZX30_D43).zip	
EBSD_05_(USAMPd13, USAMPd14, USAMPd16).zip	
EBSD_06_(USAMP_ZX31_D32,USAMP_A2d3, USAMPd3, USAMPd6, USAMPd10, ...)	
EBSD_07_(USAMP_ZX30D29, USAMP_ZX31D32).zip	
EBSD_08_(USAMP_ZX30D25, USAMP_ZX30D28).zip	
EBSD_09_(USAMP_ZX30LongD2, USAMP_ZX30D38).zip	
EBSD_10_(USAMP_ZX30D22, USAMP_ZX30D24).zip	
EBSD_11_(USAMP_ZX30D20, USAMP_ZX30D21).zip	

A more complete description of the files generated in this project can be found in [USAMP_ETL_Master_Global.xlsx](#) file included in the datahub.

Appendix II: Publications & Presentations

- T.D. Berman and J.E. Allison: “Coupling thermomechanical processing and alloy design to improve textures in Mg-Zn-Ca sheet alloys,” *JOM*, in press.
- T.D. Berman and J.E. Allison, “Texture and Microstructure Evolution in Thermomechanically Processed Mg-Ca and Mg-Zn-Ca Alloys,” oral presentation at 2021 TMS Annual Meeting & Exhibition, virtual, March 17, 2021
- T.D. Berman and J.E. Allison: “Relating Texture and Thermomechanical Processing Variables in Mg-Zn-Ca Alloys,” *Magnes. Technol.* 2020 Proc, TMS, J.B. Jordon, V. Miller, V. Joshi, and N.R. Neelameggham, eds., Springer International Publishing, 2020, 175-180.
- T.D. Berman et al., “Relating Texture and Thermomechanical Processing Variables in Mg-Zn-Ca Alloys,” oral presentation at 2020 TMS Annual Meeting & Exhibition, San Diego, CA, Feb 26, 2020.
- T.D. Berman, “Preparing Magnesium Alloys for Electron Backscatter Diffraction, poster presentation at 2020 TMS Annual Meeting & Exhibition, San Diego, CA, Feb 24, 2020.